

Unveiling the origin of steep decay in γ -ray bursts

Samuele Ronchini (✉ samuele.ronchini@gssi.it)

Gran Sasso Science Institute, Viale F. Crispi 7, 67100 L'Aquila (IT) <https://orcid.org/0000-0003-0020-687X>

Gor Oganessian

Gran Sasso Science Institute, Viale F. Crispi 7, 67100 L'Aquila (IT) <https://orcid.org/0000-0001-9765-1552>

Marica Branchesi

Gran Sasso Science Institute, Viale F. Crispi 7, 67100 L'Aquila (IT)

Stefano Ascenzi

INAF - Osservatorio Astronomico di Brera, Via E. Bianchi 46, 23807 Merate (LC), Italy

Maria Grazia Bernardini

INAF - Osservatorio Astronomico di Brera, Via E. Bianchi 46, 23807 Merate (LC), Italy

Francesco Brighenti

Gran Sasso Science Institute, Viale F. Crispi 7, 67100 L'Aquila (IT) <https://orcid.org/0000-0001-9206-8157>

Simone Dall'Osso

Gran Sasso Science Institute, Viale F. Crispi 7, 67100 L'Aquila (IT)

Paolo D'Avanzo

INAF/Brera Astronomical Observatory

Giancarlo Ghirlanda

INAF - Osservatorio Astronomico di Brera, Via E. Bianchi 46, 23807 Merate (LC), Italy
<https://orcid.org/0000-0001-5876-9259>

Gabriele Ghisellini

INAF - Osservatorio Astronomico di Brera, Via E. Bianchi 46, 23807 Merate (LC), Italy

Maria Edvige Ravasio

INAF - Osservatorio Astronomico di Brera, Via E. Bianchi 46, 23807 Merate (LC), Italy

Om Sharan Salafia

INAF - Osservatorio Astronomico di Brera, Via E. Bianchi 46, 23807 Merate (LC), Italy

Article

Keywords: Ultra-relativistic Jets, Time-resolved Spectral Analysis, Adiabatic Cooling

Posted Date: September 18th, 2020

DOI: <https://doi.org/10.21203/rs.3.rs-74350/v1>

License:  This work is licensed under a Creative Commons Attribution 4.0 International License.

[Read Full License](#)

Version of Record: A version of this preprint was published at Nature Communications on July 7th, 2021.

See the published version at <https://doi.org/10.1038/s41467-021-24246-x>.

Unveiling the origin of steep decay in γ -ray bursts

Samuele Ronchini^{1,2,3}, Gor Oganessian^{1,2,3}, Marica Branchesi^{1,2,3}, Stefano Ascenzi⁴, Maria Grazia Bernardini⁴, Francesco Brighenti¹, Simone Dall’Osso^{1,2}, Paolo D’Avanzo⁴, Giancarlo Ghirlanda^{4,5}, Gabriele Ghisellini⁴, Maria Edvige Ravasio^{4,5}, Om Sharan Salafia^{4,6}

γ -ray bursts (GRBs) are short-lived transients releasing a large amount of energy ($10^{51} - 10^{53}$ erg) in the keV-MeV energy range. GRBs are thought to originate from internal dissipation of the energy carried by ultra-relativistic jets launched by the remnant of a massive star’s death or a compact binary coalescence. While thousands of GRBs have been observed over the last thirty years, we still have an incomplete understanding of where and how the radiation is generated in the jet. A novel investigation of the GRB emission mechanism, via time-resolved spectral analysis of the X-ray tails of bright GRB pulses, enables us to discover a unique relation between the spectral index and the flux. This relation is incompatible with the long standing scenario invoked to interpret X-ray tails, that is, the delayed arrival of photons from high-latitude parts of the jet. We show that our results provide for the first time evidence of adiabatic cooling and efficient energy exchange between the emitting particles in the relativistic outflows of GRBs.

1 Introduction

The prompt emission of γ -ray bursts (GRBs) is typically followed by a steep decay phase¹ (tail) in the X-ray band. The duration of the steep decay is around $10^2 - 10^3$ s and it is characterized by a typical temporal slope of 3 – 5. Since afterglow models cannot account for such slopes, the origin of steep decay is related to the fade-off of the emission mechanism that generates the prompt phase. In order to investigate the spectral evolution during this phase, we select a sample of GRBs from the archive of the X-ray Telescope (XRT, 0.3-10 keV) on-board the Neil Gehrels Swift Observatory (Swift)². We restrict our study to a sample of GRBs (8 in total) whose brightest pulse in the Burst Alert Telescope (BAT, 15-350 keV) corresponds to the XRT peak preceding the X-ray tail (see as example the left panel in Fig. 1). We perform a time-resolved spectral analysis of the tail in the 0.5-10 keV band assuming a simple power-law model for the photon spectrum $N_\gamma \propto E^{-\alpha}$ (see Methods). We introduce a novel method for the representation of the spectral evolution plotting the photon index α as a function of the flux F integrated in the 0.5-10 keV band,

¹Gran Sasso Science Institute, Viale F. Crispi 7, I-67100, L’Aquila (AQ), Italy

²INFN - Laboratori Nazionali del Gran Sasso, I-67100, L’Aquila (AQ), Italy

³INAF - Osservatorio Astronomico d’Abruzzo, Via M. Maggini snc, I-64100 Teramo, Italy

⁴INAF – Osservatorio Astronomico di Brera, Via E. Bianchi 46, 23807 Merate (LC), Italy

⁵Università degli Studi di Milano-Bicocca, Dip. di Fisica “G. Occhialini”, Piazza della Scienza 3, 20126 Milano, Italy

⁶INFN–Sezione di Milano-Bicocca, Piazza della Scienza 3, I-20126 Milano (MI), Italy

30 hereafter referred to as the $\alpha - F$ relation. The flux is normalized to the peak value of the X-ray
31 tail. This normalization makes the result independent of the intrinsic brightness of the pulse and of
32 the distance of the GRB.

33 2 Results

34 We discover a unique $\alpha - F$ relation for the analyzed GRBs as shown in the right panel of Fig.
35 1. This is consistent with a systematic softening of the spectrum (as already observed for several
36 GRBs³); the photon index evolves from a value of $\alpha \sim 0.5 - 1$ at the peak of the XRT pulse
37 to $\alpha \sim 2 - 2.5$ at the end of the tail emission, while the flux drops by two orders of magnitude.
38 The initial and final photon indices are consistent with the typical low- and high-energy values
39 found from the analysis of the prompt emission spectrum of GRBs, namely ~ 1 and ~ 2.3 ^{4,5,6},
40 respectively. The $\alpha - F$ relation can be interpreted as being due to a spectral evolution in which
41 the spectral shape does not vary in time, but the whole spectrum is gradually shifted towards lower
42 energies while becoming progressively dimmer (see Fig. 2). The consistent spectral evolution
43 discovered in our analysis is a clear indication of a universal physical mechanism responsible for
44 the tail emission of GRBs and the corresponding spectral softening.

45 Testing High Latitude Emission

46 We first compare our results with the expectations from the high-latitude emission (HLE)^{7,8,9,10},
47 which is the widely adopted model for interpreting the X-ray tails of GRBs. When the emission
48 from a curved surface is switched off, an observer receives photons from increasing latitudes with
49 respect to the line of sight. The higher the latitude, the lower the Doppler factor, resulting in a
50 shift towards lower energies of the spectrum in the observer frame. Through an accurate modeling
51 of HLE (as described in Methods) we derive the predicted $\alpha - F$ relation. We first consider a
52 smoothly broken power-law (SBPL) comoving spectrum. Regardless of the choice of the peak
53 energy, the bulk Lorentz factor or the radius of the emitting surface, the HLE predicts an $\alpha - F$
54 relation whose rise is shallower than the observed one (right panel of Fig. S1 in Supplementary
55 materials). We additionally test the Band function, commonly adopted for GRB spectra¹¹, and the
56 physically motivated synchrotron spectrum¹², obtaining similar results (Fig. S2 and left panel of
57 Fig. S3 in Supplementary Materials): the HLE softening is too slow to account for the observed
58 $\alpha - F$ relation. We further relax the assumption of an infinitesimal duration pulse, i.e. considering
59 a shell that is continuously emitting during its expansion and suddenly switches off at radius R_0 ¹³
60 (see Methods). The contributions from regions $R < R_0$ are sub-dominant with respect to the
61 emission coming from the last emitting surface at $R = R_0$, resulting in a spectral evolution still
62 incompatible with the observations (Fig. S4). An interesting alternative is the HLE emission from
63 an accelerating region¹⁴ taking place in some Poynting flux dissipation scenarios¹⁵. Even though it
64 can explain the temporal slopes observed in the X-ray tails, also this scenario fails in reproducing
65 the $\alpha - F$ relation (see Fig. S5 in Supplementary materials). Our results on HLE are based on
66 the assumption of a common comoving spectrum along the entire jet core. Even changing the
67 curvature (or sharpness) of the spectrum or assuming a latitude dependence of the spectral shape,

68 the disagreement with the data remains, unless we adopt a very fine-tuned structure of the spectrum
 69 along the jet core, which is not physically motivated (see Methods). Alternative models, such as
 70 anisotropic jet core or sub-photospheric dissipation, can hardly reproduce our results (see Methods).

71 **Adiabatic cooling**

72 Since the standard HLE and its modified versions, as well as alternative scenarios, are not able to
 73 robustly interpret the observed $\alpha - F$ relation, we consider a mechanism based on an intrinsic evo-
 74 lution of the comoving spectrum. The most natural process is the adiabatic cooling of the emitting
 75 particles¹⁶. Here we assume conservation of the entropy of the emitting system $\langle \gamma \rangle^3 V'$ throughout
 76 its dynamical evolution, where $\langle \gamma \rangle$ is the average random Lorentz factor of the emitting particles
 77 and $V' \propto R^2 \Delta R'$ the comoving volume¹⁷. We consider both thick and thin emitting regions, i.e.
 78 a comoving thickness of the emitting shell $\Delta R' = \text{const}$ or $\Delta R' \propto R$, respectively. We assume a
 79 power law radial decay of the magnetic field $B = B_0 (R/R_0)^{-\lambda}$, with $\lambda > 0$, and synchrotron radi-
 80 ation as the dominant emission mechanism. Here R_0 is the radius at which adiabatic cooling starts
 81 to dominate the evolution of the emitting particles. We compute the observed emission taking also
 82 into account the effect of HLE by integrating the comoving intensity along the equal arrival time
 83 surfaces (see Methods). In this scenario, contrary to HLE alone, the emission from the jet is not
 84 switched off suddenly, but the drop in flux and the spectral evolution are produced by a gradual
 85 fading and softening of the source, driven by adiabatic cooling of particles. The resulting spectral
 86 evolution and light curves are shown in Fig. 3.

87 Adiabatic cooling produces a much faster softening of α as a function of the flux decay, with re-
 88 spect to HLE alone, in agreement with the data. Adopting an initial peak frequency $\nu_p = 100$
 89 keV, the $\alpha - F$ relation is well reproduced for values $0.2 \lesssim \lambda \lesssim 0.8$, which are smaller than those
 90 expected in an emitting region with a transverse magnetic field ($\lambda = 1$ or $\lambda = 2$ for a thick or a thin
 91 shell, respectively) or magnetic field in pressure equilibrium with the emitting particles ($\lambda = 4/3$
 92 or $\lambda = 2$ for a thick or a thin shell, respectively¹⁷). Decreasing the observed initial peak frequency,
 93 the curves become steeper especially in the initial part of the decay. On the other hand, assuming a
 94 different evolution of the shell thickness, the behavior of the curves changes only marginally. For
 95 large values of λ the evolution of α flattens in the late part of the decay (see Fig. 3), indicating
 96 that the spectral evolution becomes dominated by the emission at larger angles, rather than by adi-
 97 abatic cooling in the jet core. For the same values of λ , adiabatic cooling can also well reproduce
 98 the light curve of X-ray tails (right Panel of Fig. 3). For comparison, in the same plot we show
 99 the light curve given by pure HLE, adopting the same value of R_0 and Γ . The typical timescale
 100 of adiabatic cooling $\tau_{ad} = R_0/2c\Gamma^2$, i.e. the observed time interval during which the radius dou-
 101 bles, is equal to the HLE timescale^{7,18} and radically affects the slope of X-ray tails. Therefore, the
 102 comparison between the model and the observed light curves allows us to constrain the size R_0 of
 103 the emitting region as in HLE^{19,20}. Assuming the same range of λ derived before from the $\alpha - F$
 104 relation, we find values in the range $0.8 \text{ s} \lesssim \tau_{ad} \lesssim 8 \text{ s}$ produce a good agreement with the data and
 105 are marginally consistent with the typical duration of GRB pulses ($< 1 \text{ sec}$ ²¹). This implies a size
 106 $5 \times 10^{14} (\Gamma/100)^2 \text{ cm} \lesssim R_0 \lesssim 5 \times 10^{15} (\Gamma/100)^2 \text{ cm}$ for the emission site. A different prescription
 107 for adiabatic cooling has been suggested in the literature¹⁶, in which the particle's momentum gets
 108 dynamically oriented transverse to the direction of the local magnetic field. In this case, HLE is

109 the dominant contributor to the X-ray tail emission, which is again incompatible with the observed
110 $\alpha - F$ relation. From our work we conclude that the energy of the emitting particles should be
111 necessarily coupled at the micro-physical level with the magnetic field to provide the ideal gas
112 prescription of a constant entropy¹⁶.

113 **Extending the sample**

114 In order to further test the solidity of the $\alpha - F$ relation, we extend our analysis to a second sample
115 of GRBs (composed by 8 elements) which present directly a steep decay at the beginning of the
116 XRT light curve, instead of an X-ray pulse (see left panel of Fig. 4), often observed in early X-
117 ray afterglows^{22,23}. We require that the XRT steep decay is preceded by a pulse in the BAT light
118 curve (the brightest since its trigger time). We add the data of this second sample to the $\alpha - F$
119 plot, estimating the peak flux by the extrapolation of the XRT light curve backwards to the peak
120 time of the BAT pulse, under the assumption that BAT peak and XRT peak were simultaneous
121 (see Methods). We find that these GRBs follow the overall $\alpha - F$ relation (right panel of Fig. 4),
122 confirming the universal nature of the physical process governing the spectral evolution of X-ray
123 tails. Adiabatic cooling is still capable of reproducing the data of this second sample (see left panel
124 of Fig. S1), provided we assume a slightly softer high energy intrinsic spectrum ($\alpha \sim 3$ instead of
125 $\alpha \sim 2.5$, as used in Fig. 3). We specify that the samples considered in this work are representative
126 of usual prompt emission phase and their limited size is related to the adopted requirements, which
127 are necessary for an appropriate time-resolved spectral analysis.

128 **3 Conclusions**

129 The $\alpha - F$ relation, discovered in our analysis, requires a mechanism that produces the X-ray
130 tails of GRBs with a unique law of flux decay and spectral softening. We find that adiabatic cool-
131 ing of the emitting particles, together with a slowly decaying magnetic field, robustly reproduces
132 this relation. Our results suggest an efficient coupling between a slowly decaying magnetic field
133 and the emitting particles. The adiabatic cooling should dominate over radiative cooling, other-
134 wise most of the internal energy would be radiated away before the system expands substantially.
135 This may be an indication of intrinsically inefficient emitting particles in GRB outflows, such as
136 protons²⁴, since the electron cooling timescale τ_{e-} in a compact and highly magnetized ejecta is
137 catastrophically short ($\tau_{e-} \ll 1$ s²⁵). Our findings are generally in agreement with moderately
138 fast and slow cooling regimes of the synchrotron radiation, which is able to reproduce the overall
139 GRB spectral features²⁶. However, our results disfavor models with re-acceleration/slow heating of
140 electrons^{27,28}, since when electrons are left unenergized we would again observe HLE-dominated
141 X-ray tails. In conclusion, our results show that adiabatic cooling plays a crucial role for the col-
142 lective evolution of the radiating particles in GRB outflows and consequently for the determination
143 of spectral and temporal properties of prompt emission episodes. The coupling between particles
144 and magnetic field ensures the intrinsic nature and hence the universality of this process, whose
145 effects are independent of the global properties of the system, such as the luminosity of the GRB
146 or the geometry of the jet.

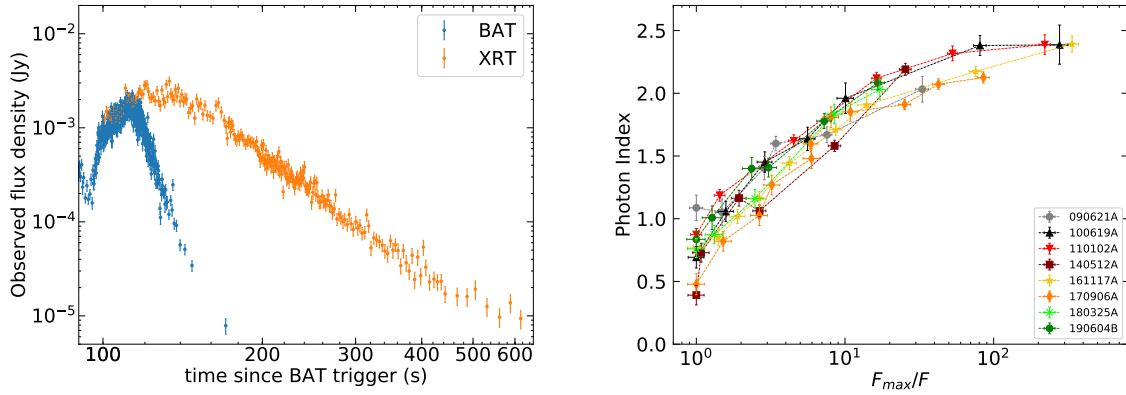


Figure 1: **Left panel:** An example of a light curve of an X-ray tail selected from our sample, taken from the GRB 161117A. We show on the same plot the XRT (orange) and the BAT (blue) flux density at 1 keV and 50 keV, respectively. **Right panel:** Spectral evolution of the X-ray tail for all the GRBs in the first sample (shown with different colors). The photon index α is represented as a function of the reciprocal of the normalized flux F_{max}/F . Time flows from left to right.

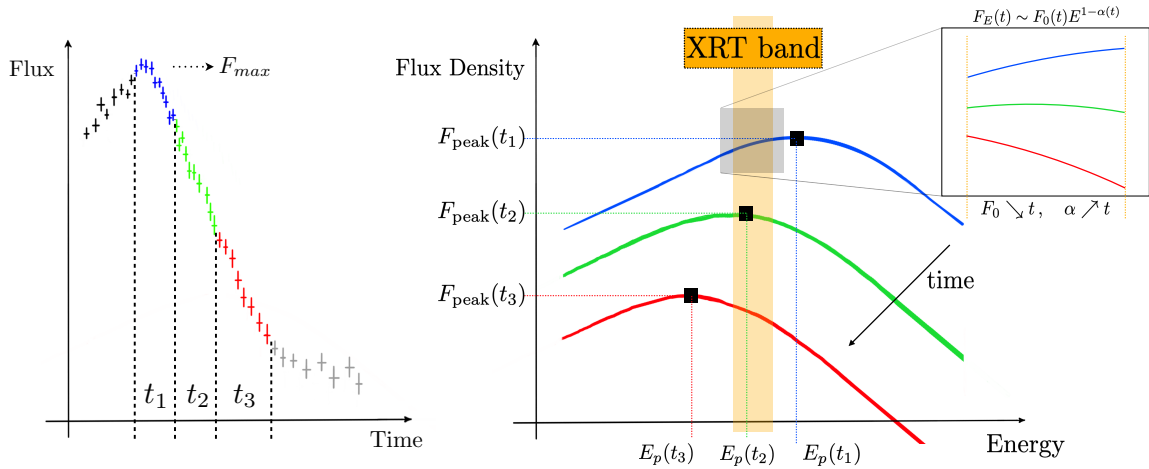


Figure 2: Illustration of the spectral evolution caused by a shift of the spectrum towards lower energies. The transition of the spectral peak through the XRT band explains the observed spectral softening. Since in the right panel we plot the flux density, the local slope in the XRT band is given by $1 - \alpha$, where α is the photon index.

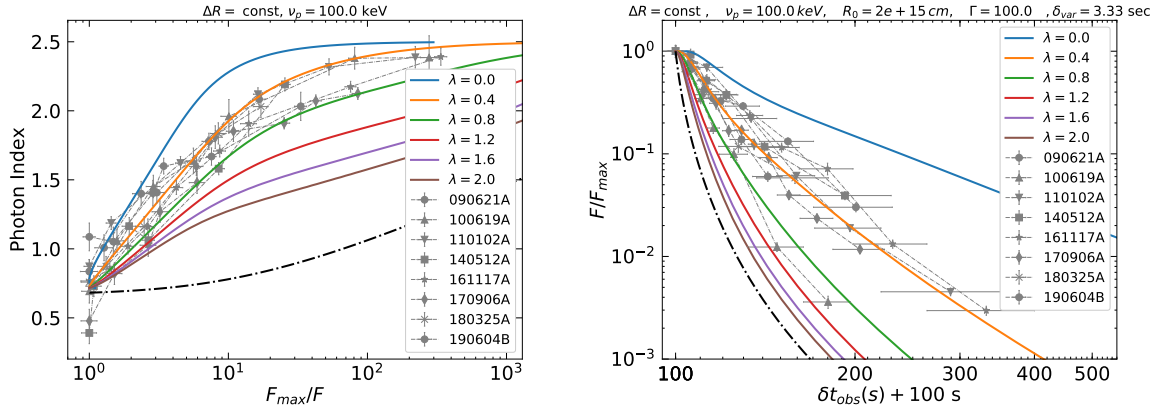


Figure 3: **Left panel:** Spectral evolution expected in the case of adiabatic cooling (solid lines). The theoretical curves are computed taking also into account the effect of HLE. The value of λ specifies the evolution of the magnetic field. We adopt a SBPL as spectral shape with $\alpha_s = -1/3$ and $\beta_s = 1.5$, an initial observed peak frequency of 100 keV and a thickness of the expanding shell that is constant in time. The dot-dashed line is the evolution expected in case of HLE without adiabatic cooling, assuming the same spectral shape and initial observed peak frequency. **Right panel:** Temporal evolution of normalized flux expected in case of adiabatic cooling. $\delta t_{obs} + 100$ s is the time measured from the peak of the decay shifted at 100 s, the typical starting time of the tail emission detected by XRT. We adopt the same parameters as in the left panel, assuming $R_0 = 2 \times 10^{15}$ cm and $\Gamma = 100$. The dot-dashed line is the corresponding HLE model without accounting for adiabatic cooling. $\delta_{var} = R_0/2c\Gamma^2$ indicates the timescale of adiabatic cooling, which is the same of HLE.

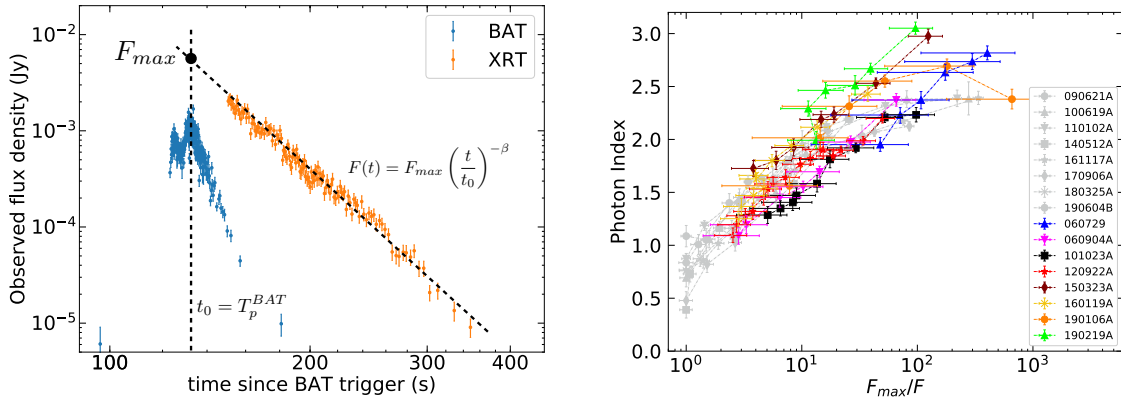


Figure 4: **Left panel:** An example of a light curve of an X-ray tail selected for our second sample, taken from GRB 150323A. We report on the same plot the XRT (orange) and the BAT (blue) flux density at 1 keV and 50 keV, respectively. The peak flux F_{max} is estimated extrapolating the X-ray tail back to the BAT peak. **Right panel:** Spectral evolution of our extended sample of GRBs, which present a steep decay at the beginning of the XRT light curve, preceded by the brightest BAT pulse since the trigger time. The evolution of α lies on the same region of the plane occupied by the original sample, indicated in grey.

References

1. Nousek, J. A., and 27 colleagues 2006. Evidence for a Canonical Gamma-Ray Burst Afterglow Light Curve in the Swift XRT Data. *The Astrophysical Journal* 642, 389.
2. Gehrels, N., and 70 colleagues 2004. The Swift Gamma-Ray Burst Mission. *The Astrophysical Journal* 611, 1005.
3. Zhang, B.-B., Liang, E.-W., & Zhang, B. 2007. A Comprehensive Analysis of Swift XRT Data. I. Apparent Spectral Evolution of Gamma-Ray Burst X-Ray Tails *The Astrophysical Journal*, 666, 1002
4. Frontera, F., and 16 colleagues 2000. Prompt and Delayed Emission Properties of Gamma-Ray Bursts Observed with BeppoSAX. *The Astrophysical Journal Supplement Series* 127, 59.
5. Kaneko, Y., Preece, R. D., Briggs, M. S., Paciesas, W. S., Meegan, C. A., Band, D. L. 2006. The Complete Spectral Catalog of Bright BATSE Gamma-Ray Bursts. *The Astrophysical Journal Supplement Series* 166, 298.
6. Nava, L., Ghirlanda, G., Ghisellini, G., Celotti, A. 2011. Spectral properties of 438 GRBs detected by Fermi/GBM. *Astronomy and Astrophysics* 530, A21.
7. Fenimore, E. E., Madras, C. D., Nayakshin, S. 1996. Expanding Relativistic Shells and Gamma-Ray Burst Temporal Structure. *The Astrophysical Journal* 473, 998.
8. Kumar, P., Panaitescu, A. 2000. Afterglow Emission from Naked Gamma-Ray Bursts. *The Astrophysical Journal* 541, L51.
9. Zhang, B., and 7 colleagues 2006. Physical Processes Shaping Gamma-Ray Burst X-Ray Afterglow Light Curves: Theoretical Implications from the Swift X-Ray Telescope Observations. *The Astrophysical Journal* 642, 354.
10. Liang, E. W., and 17 colleagues 2006. Testing the Curvature Effect and Internal Origin of Gamma-Ray Burst Prompt Emissions and X-Ray Flares with Swift Data. *The Astrophysical Journal* 646, 351.
11. Band, D., and 14 colleagues 1993. BATSE Observations of Gamma-Ray Burst Spectra. I. Spectral Diversity. *The Astrophysical Journal* 413, 281.
12. Rees, M. J., Meszaros, P. 1994. Unsteady Outflow Models for Cosmological Gamma-Ray Bursts. *The Astrophysical Journal* 430, L93.
13. Genet, F., Granot, J. 2009. Realistic analytic model for the prompt and high-latitude emission in GRBs. *Monthly Notices of the Royal Astronomical Society* 399, 1328.
14. Uhm, Z. L., Zhang, B. 2015. On the Curvature Effect of a Relativistic Spherical Shell. *The Astrophysical Journal* 808, 33.

- 182 15. Zhang, B., Yan, H. 2011. The Internal-collision-induced Magnetic Reconnection and Turbu-
183 lence (ICMART) Model of Gamma-ray Bursts. *The Astrophysical Journal* 726, 90.
- 184 16. Barniol Duran, R., Kumar, P. 2009. Adiabatic expansion, early X-ray data and the central
185 engine in GRBs. *Monthly Notices of the Royal Astronomical Society* 395, 955.
- 186 17. Mészáros, P., Rees, M. J. 1999. GRB 990123: reverse and internal shock flashes and late
187 afterglow behaviour. *Monthly Notices of the Royal Astronomical Society* 306, L39.
- 188 18. Sari, R., Piran, T. 1997. Variability in Gamma-Ray Bursts: A Clue. *The Astrophysical Journal*
189 485, 270.
- 190 19. Lyutikov, M. 2006. Did Swift measure gamma-ray burst prompt emission radii?. *Monthly*
191 *Notices of the Royal Astronomical Society* 369, L5.
- 192 20. Lazzati, D., Begelman, M. C. 2006. Thick Fireballs and the Steep Decay in the Early X-Ray
193 Afterglow of Gamma-Ray Bursts. *The Astrophysical Journal* 641, 972.
- 194 21. Walker, K. C., Schaefer, B. E., Fenimore, E. E. 2000. Gamma-Ray Bursts Have Millisecond
195 Variability. *The Astrophysical Journal* 537, 264.
- 196 22. Tagliaferri, G., and 34 colleagues 2005. An unexpectedly rapid decline in the X-ray afterglow
197 emission of long γ -ray bursts. *Nature* 436, 985.
- 198 23. O'Brien, P. T., and 31 colleagues 2006. The Early X-Ray Emission from GRBs. *The Astro-*
199 *physical Journal* 647, 1213.
- 200 24. Ghisellini, G., and 8 colleagues 2020. Proton-synchrotron as the radiation mechanism of the
201 prompt emission of gamma-ray bursts?. *Astronomy and Astrophysics* 636, A82.
- 202 25. Ghisellini, G., Celotti, A., Lazzati, D. 2000. Constraints on the emission mechanisms of
203 gamma-ray bursts. *Monthly Notices of the Royal Astronomical Society* 313, L1.
- 204 26. Zhang, B. 2020. Synchrotron radiation in γ -ray bursts prompt emission. *Nature Astronomy* 4,
205 210.
- 206 27. Asano, K., Terasawa, T. 2009. Slow Heating Model of Gamma-ray Burst: Photon Spectrum
207 and Delayed Emission. *The Astrophysical Journal* 705, 1714.
- 208 28. Beniamini, P., Barniol Duran, R., Giannios, D. 2018. Marginally fast cooling synchrotron
209 models for prompt GRBs. *Monthly Notices of the Royal Astronomical Society* 476, 1785.

210 **Acknowledgements** MB, SDO, GO acknowledge financial contribution from the agreement ASI-
211 INAF n.2017-14-H.0. The research leading to these results has received funding from the European
212 Union’s Horizon 2020 Programme under the AHEAD2020 project (grant agreement n. 871158).
213 SA acknowledges the PRIN-INAF ”Towards the SKA and CTA era: discovery, localization and
214 physics of transient sources”. MGB and PDA acknowledge ASI grant I/004/11/3. OS acknowl-
215 edges the INAF-Prin 2017 (1.05.01.88.06) and the Italian Ministry for University and Research
216 grant “FIGARO” (1.05.06.13) for support. GO and SR are thankful to INAF – Osservatorio Astro-
217 nomico di Brera for kind hospitality during the completion of this work. This work made use of
218 data supplied by the UK Swift Science Data Centre at the University of Leicester.

219 **Competing Interests** The authors declare no competing interests

220 Methods

221 **Sample selection.** We define the steep decay (SD) segment^{1,9,22,23} as the portion of the light curve
222 that is well approximated by a power law, $F \propto t^{-\alpha}$ with $\alpha > 2$. Such criterion allow us to exclude
223 a decay coming from a forward shock^{29,30,31}. In order to determine the presence of a SD, we
224 analyze the light curve of the integrated flux in the XRT $E = 0.3 - 10$ keV band.
225 From the Swift catalog³² as of the end of 2019, we selected all GRBs with an XRT peak flux
226 $F_p^{XRT} > 10^{-8}$ erg cm⁻²s⁻¹. We selected the brightest pulses in order to have a good enough
227 spectral quality as to perform a time resolved spectral analysis. The peak flux is computed taking
228 the maximum of $F(t_i)$, where $F(t_i)$ are the points of the light curve at each time t_i (the light curve
229 data are taken at this link [https://www.swift.ac.uk/xrt_curves/GRB_ID/flux.](https://www.swift.ac.uk/xrt_curves/GRB_ID/flux.qdp)
230 [qdp](https://www.swift.ac.uk/xrt_curves/GRB_ID/flux.qdp), where GRB_ID is the GRB observation ID). Among these GRBs, we selected our first sample
231 according to the following criteria:

- 232 1. The XRT light curve shows at least one SD segment that is clean, i.e. without secondary
233 peaks or relevant fluctuations.
- 234 2. If we call F_1 and F_2 the fluxes at the beginning and at the end of the SD, respectively, we
235 require that $\frac{F_1}{F_2} > 10$. This requirement is necessary to have a sufficient number of temporal
236 bins inside the SD segment and therefore a well sampled spectral evolution.
- 237 3. The beginning of the SD phase corresponds to a peak in the XRT light curve, such that
238 we have a reliable reference for the initial time. We stress that the identification of the SD
239 starting time in XRT is limited by the observational window of the instrument. This means
240 that, if the XRT light curve starts directly with a SD phase, with no evidence of a peak, the
241 initial reference time is possibly located before and its value cannot be directly derived.
- 242 4. The XRT peak before the SD has a counterpart in BAT, whose peak is the brightest since
243 the trigger time. This requirement is necessary to ensure that XRT is looking at a prompt
244 emission episode, whose typical peak energy is above 100 keV. In a quantitative way, we
245 define two times, t_p and t_{90}^{stop} , where the first indicates the beginning of the peak that gener-
246 ates the SD, while the second is the end time of T_{90} ³³, with respect to the trigger time. We
247 require $t_{90}^{stop} > t_p$ in order to have an overlap between the last prompt pulses (monitored by
248 BAT) and the XRT peak that precedes the SD phase. Namely, such requirement ensures that
249 a considerable fraction of the energy released by the burst goes into the pulse that generates
250 the X-ray tail.

251 It is possible that more than one peak is present in the XRT light curve, each with a following SD.
252 In this case we consider only the SD after the brightest peak. If two peaks have a similar flux, we
253 consider the SD with the larger value of $\frac{F_1}{F_2}$.

254 We define then a second sample of GRBs that satisfy the first two points listed before, but have a

255 SD at the beginning of the XRT light curve, namely no initial peak preceding the SD is present. In
 256 addition, we require that a BAT pulse precedes the XRT SD and is the brightest since the trigger
 257 time. The BAT pulse enables us to constrain the starting of the SD.

258 **Time resolved spectral analysis.** For each GRB we divided the XRT light curve in several time
 259 bins, according to the following criteria:

- 260 1. Each bin contains only data in Windowed Timing (WT) mode or in Photon Counting (PC)
 261 mode, since mixed WT+PC data cannot be analyzed as a single spectrum.
2. Each bin contains a total number of counts N_{bin} in the $E = 0.3 - 10$ keV band larger than a
 certain threshold N_0 , which is chosen case by case according to the brightness of the source.
 The definition of the time bins is obtained by an iterative process, i.e. starting from the first
 point of the light curve we keep including subsequent points until

$$N_{bin} = \sum_{t_n=t_i}^{t_f} N(t_n) > N_0$$

262 where $N(t_n)$ are the counts associated to each point of the light curve, while t_i and t_f define
 263 the starting and ending time of the bin. Then the process is repeated for the next bins, until
 264 t_f is equal to the XRT ending time. Due to the large range of count rates covered during a
 265 typical XRT light curve, the choice of only one value for N_0 would create an assembly of
 266 short bins at the beginning and too long bins toward the end. Therefore we use one value of
 267 N_0 for bins in WT mode (N_0^{WT}) and a smaller value of N_0 for bins in PC mode (N_0^{PC}). In
 268 our sample, the SD is usually in observed in WT mode, therefore we adjust N_0^{WT} in order
 269 to have at least 4-5 bins inside the SD. A typical value of N_0^{WT} is around 1500-3000, while
 270 N_0^{PC} is around 500-1000. Using these values, we verified that the relative errors of photon
 271 index and normalization resulting from spectral analysis are below $\sim 30\%$.

3. For each couple (N_i, N_j) of points inside the bin, the following relation must hold:

$$\frac{|N_i - N_j|}{\sqrt{\sigma_i^2 + \sigma_j^2}} < 5$$

272 where σ_i and σ_j are the associated errors. Such requirement avoids large flux variations
 273 within the bin itself.

- 274 4. The duration of the bin is larger than 5 seconds, in order to avoid pileup in the automati-
 275 cally produced XRT spectra, obtained from the website [https://www.swift.ac.uk/
 276 xrt_spectra/addspec.php?targ=GRB_ID](https://www.swift.ac.uk/xrt_spectra/addspec.php?targ=GRB_ID), where `GRB_ID` is the ID number of
 277 the GRB.

278 It is possible that condition 3 is satisfied only for a duration of the bin $T_{bin} < T_0$, while condition
 279 2 is satisfied for $T_{bin} > T_0^*$, but $T_0^* > T_0$, meaning that they cannot be satisfied at the same time.
 280 In this case, we give priority to condition 3, provided that N_{bin} is not much smaller than N_0 .
 281 Due to the iterative process that defines the duration of the bins, it is possible that the last points in
 282 WT and PC mode are grouped in a single bin with a too small N_{bin} , giving a too noisy spectrum.
 283 Therefore, they are excluded from the spectral analysis.

284 **Spectral modeling.** The spectrum of each bin is obtained using the automatic online tool provided
 285 by Swift for spectral analysis (https://www.swift.ac.uk/xrt_spectra/addspec.php?targ=GRB_ID, where GRB_ID is the ID number of the GRB). The details of the automatic
 286 spectral analysis can be found here https://www.swift.ac.uk/xrt_spectra/docs.php#filespec. Each spectrum is analyzed using XSPEC³⁴, version 12.10.1, and the Python
 287 interface PyXspec. We discard all photons with energy $E < 0.5$ keV and $E > 10$ keV. The spectra
 288 are modeled with an absorbed power law and for the absorption we adopted the Tuebingen-Boulder
 289 model³⁵. If the GRB redshift is known, we use two distinct absorbers, one Galactic³⁶ and one
 290 relative to the host galaxy (the XSPEC syntax is *tbabs*ztbabs*po*). The column density N_H of the
 291 second absorber is estimated through the spectral analysis, as explained below. On the other hand,
 292 if the GRB redshift is unknown, we model the absorption as a single component located at redshift
 293 $z=0$ (the XSPEC syntax is *tbabs*po*) and also in this case the value of N_H is derived from spectral
 294 analysis.

295 For the estimation of the host N_H we consider only the late part of the XRT light curve following
 296 the SD phase. At late time with respect to the trigger we do not expect strong spectral evolution,
 297 as verified in several works in the literature^{37,38}. Therefore, for each GRB, the spectrum of each
 298 bin after the SD is fitted adopting the same N_H which is left free during the fit. Normalization and
 299 photon index are also left free, but they have different values for each spectrum. We call N_H^{late} the
 300 value of N_H obtained with this procedure. In principle the burst can affect the ionization state of
 301 the surrounding medium, but we assume that such effects are negligible and N_H does not change
 302 dramatically across the duration of the burst³⁹. Hence we analyzed separately all the spectra of the
 303 SD using a unique value of $N_H = N_H^{late}$, which is fixed during the fit. Normalization and photon
 304 index, instead, are left free.

305 An alternative method for the derivation of N_H is the fitting of all the spectra simultaneously
 306 imposing a unique value of N_H that is left free. On the other hand, since N_H and photon index are
 307 correlated, an intrinsic spectral evolution can induce an incorrect estimation of N_H . For the same
 308 reason we do not fit the spectra adopting a free N_H , since we would obtain an evolution of photon
 309 index strongly affected by the degeneracy with N_H .

310 In this regard, we tested how our result about spectral evolution depend on the choice of N_H . On
 311 average we found that the fits of the SD spectra remain good ($stat/dof \lesssim 1$) for a variation of
 312 N_H of about 50%. As a consequence, the photon index derived by the fit would change at most of
 313 30%. Therefore the error bars reported in all the plots $\alpha - F$ are possibly under-estimated, but even
 314 considering a systematic error that corresponds to $\sim 30\%$ of the value itself would not undermine
 315 the solidity of the results.

Extrapolation of F_{max} . We explain here how we extrapolated the F_{max} for the GRBs of the second sample, for which the XRT light curve starts directly with a SD. We consider the peak time T_p^{BAT} of the BAT pulse that precedes the SD. In the assumption that the SD starts at T_p^{BAT} , we can derive F_{max} using the following procedure. We consider the 0.5-10 keV flux $F(t_i)$ for each bin time t_i in the SD, derived from spectral analysis. Then we fit these points with a power law

$$F(t_i) = F_{max} \left(\frac{t_i}{t_0} \right)^{-\beta}$$

318 with $\beta > 0$ and imposing that $t_0 = T_p^{BAT}$. Finally we derive the best fit value of F_{max} with the
 319 associated 1σ error. The error of F_{max} has a contribution coming from the error associated to β
 320 and another associated to t_0 , as well as from the assumption of a power law as fitting function. The
 321 value of T_p^{BAT} is obtained fitting the BAT pulse with a Gaussian profile. Since usually the BAT
 322 pulse can have multiple sub-peaks and taking also into account possible lags between XRT and
 323 BAT peaks, we adopt a conservative error associated to T_p^{BAT} equal to 5 seconds.

324 **High Latitude Emission.** We assume that an infinitesimal duration pulse of radiation is emitted
 325 on the surface of a spherical shell, at radius R_0 from the center of the burst. The jet has an aperture
 326 angle ϑ_j and it expands with a bulk Lorentz factor Γ . We assume also that the comoving spectrum
 327 is the same on the whole jet surface. The temporal evolution of the observed flux density is given
 328 by⁴⁰:

$$F_\nu(t_{obs}) \propto S_{\nu'}(\nu/\mathcal{D}(\vartheta)) \mathcal{D}^2(\vartheta) \cos(\vartheta) \quad (1)$$

329 with $S_{\nu'}(\nu/\mathcal{D}(\vartheta))$ the comoving spectral shape, $\mathcal{D}(\vartheta)$ the Doppler factor and ϑ the angle measured
 330 from the line of sight, which is assumed to coincide with the jet symmetry axis. The observer time
 331 t_{obs} is related to the angle ϑ through this formula:

$$t_{obs}(\vartheta) = t_{em}(1 - \beta \cos \vartheta) \quad (2)$$

332 where t_{em} is the emission time. Eq. (1) is valid for $\vartheta < \vartheta_j$, while for $\vartheta > \vartheta_j$ the emission drops to
 333 zero. This implies that for $t_{obs} > t_{em}(1 - \beta \cos \vartheta_j)$ the flux drops to zero. At each time $t_{obs}(\vartheta)$ the
 334 observer receives a spectrum that is Doppler shifted by a factor $\mathcal{D}(\vartheta)$ with respect to the comoving
 335 spectrum. If the comoving spectrum is curved, i.e. if $\frac{d^2}{d\nu'^2} S_{\nu'} \neq 0$, then also the photon index is
 336 a function of time⁴¹. The shape of the resulting curve $\alpha - F$ is determined only by the spectral
 337 shape and the comoving peak frequency ν'_p , while it is independent on the emission radius R_0 and
 338 the bulk Lorentz factor Γ .

339 We notice that the observed photon index goes from 0.5 – 1.0 up to 2.0 – 2.5, consistent with
 340 the slopes of a synchrotron spectrum before and after the peak frequency. Indeed for a population
 341 of particles with an injected energy distribution $N(\gamma) \propto \gamma^{-p}$ that has not completely cooled, the
 342 expected shape of the spectrum is $F_\nu \sim \nu^{1/3}$ ($\alpha = 2/3$) for $\nu < \nu_c$ and $F_\nu \sim \nu^{-p/2}$ ($\alpha = p/2 + 1$)
 343 for $\nu > \nu_m \gtrsim \nu_c$. Hereafter, if not otherwise specified, we assume a spectral shape given by a
 344 smoothly broken lower law, which well approximates the synchrotron spectrum below and above

345 the peak frequency. The form of the adopted spectral shape is

$$S_\nu \propto \frac{1}{\left(\frac{\nu}{\nu_0}\right)^{\alpha_s} + \left(\frac{\nu}{\nu_0}\right)^{\beta_s}} \quad (3)$$

346 with $\alpha_s = -1/3$ and $\beta_s = 1.5$. The peak frequency ν_p of the energy spectrum νS_ν is related to ν_0
 347 through the following relation:

$$\nu_p = \left(-\frac{2 + \alpha}{2 + \beta}\right)^{\frac{1}{\alpha - \beta}} \nu_0 \quad (4)$$

348 At each arrival time we compute the flux and the photon index in the XRT band using eq. (1). In
 349 particular, the XRT flux is given by

$$F_{0.5-10 \text{ keV}}(t_{obs}) = \int_{0.5 \text{ keV}/h}^{10 \text{ keV}/h} F_\nu(t_{obs}) d\nu \quad (5)$$

350 where h is Planck's constant, while the photon index is computed as^{13,41}

$$\alpha(t_{obs}) = 1 - \frac{\log [F_{\nu=10 \text{ keV}/h}(t_{obs}) / F_{\nu=0.5 \text{ keV}/h}(t_{obs})]}{\log (10 \text{ keV} / 0.5 \text{ keV})} \quad (6)$$

351 This method for the evaluation of photon index is valid in the limit of a spectrum that can be always
 352 approximated with a power law as it passes through the XRT band, which is the case for typical
 353 prompt emission spectra.

354 In addition to the SBPL, we test HLE also using other spectral shapes. We first adopt a Band
 355 function¹¹ with the following form:

$$B(\epsilon) = \begin{cases} \epsilon^{1+\alpha} e^{-\epsilon} & \epsilon < \alpha - \beta \\ (\alpha - \beta)^{\alpha - \beta} e^{-\alpha + \beta} \epsilon^{1+\beta} & \epsilon > \alpha - \beta \end{cases} \quad (7)$$

356 where $\epsilon = \nu/\nu_0$. In this case the peak of the energy spectrum is at $\nu_p = (2 + \alpha)\nu_0$. The resulting
 357 spectral evolution is very similar to the case of SBPL, as visible in left panel of Fig. S3.

358 As a final attempt, we use synchrotron spectrum emitted by a population of particles with an initial
 359 energy distribution $N(\gamma) \propto \gamma^{-p}$. Synchrotron is considered the dominant radiative process in
 360 prompt emission of GRBs^{12,26}. In the fast cooling regime, the particle distribution becomes

$$N(\gamma) \propto \begin{cases} \gamma^{-2} & \gamma_c < \gamma < \gamma_m \\ \gamma^{-(p+1)} & \gamma > \gamma_m \end{cases} \quad (8)$$

361 The only three parameters that define the shape of the synchrotron spectrum are $\nu_m \propto \gamma_m^2$, $\nu_c \propto \gamma_c^2$
 362 and p . For the computation of the spectrum we use⁴²:

$$F_\nu \propto \int_{\gamma_c}^{\infty} P(\nu, \gamma) N(\gamma) d\gamma \quad (9)$$

363 with

$$P(\nu, \gamma) \propto B \left[\left(\frac{\nu}{\nu_{ch}} \right) \int_{\frac{\nu}{\nu_{ch}}}^{\infty} K_{5/3}(x) dx \right], \quad \nu_{ch} \propto \gamma^2 B \quad (10)$$

364 where B is the magnetic field and $K_{5/3}(x)$ is the modified Bessel function of order 5/3. The
 365 resulting spectral evolution for values of $\nu_m/\nu_c = 1$ and $\nu_m/\nu_c = 10$ is reported in Fig. S2. A
 366 value of $\nu_m/\nu_c \sim 1$ is expected in the marginally fast cooling regime^{43,44,45}, which is favored by
 367 broad-band observations of GRB prompt spectra^{46,47,48,49,50,51}. Finally we test how the sharpness of
 368 the spectral peak can affect our results. In particular we consider again a SBPL and we generalize
 369 the formula adding a sharpness parameter n :

$$S_{\nu}^{(n)} \left(\frac{\nu}{\nu_0} \right) \propto \left[\frac{1}{\left(\frac{\nu}{\nu_0} \right)^{n\alpha_s} + \left(\frac{\nu}{\nu_0} \right)^{n\beta_s}} \right]^{1/n} \quad (11)$$

370 where larger values of n correspond to sharper spectral peaks. As visible in right panel of Fig. S3,
 371 where we have adopted $n = 4$, the shape of the curves becomes flatter at the beginning and at the
 372 end of the decay, but with no substantial steepening of the intermediate part. This is attributable
 373 to HLE that imposes an evolution of the observed peak frequency like t_{obs}^{-1} . Thus, while the initial
 374 and final values of photon index are dictated by the spectral shape, the steepness of the transition
 375 from the initial to the final value is governed by HLE and is independent on the spectral shape. In
 376 conclusion, no one of the alternative spectral shapes that we tested is able to reconcile HLE with
 377 the observed spectral evolution.

378 We finally test how the $\alpha - F$ relation changes if we assume a structured jet with an angle-
 379 dependent comoving spectrum. In particular, we consider a spectral peak energy that is nearly
 380 constant inside an angle ϑ_c (measured with respect to the line of sight) and starts to decrease out-
 381 side it. Regardless of the choice of the specific law for the angular dependence (e.g. Gaussian
 382 or power law), the HLE can reproduce the $\alpha - F$ relation only if all the analyzed GRBs have a
 383 fine-tuned value of $\vartheta_c < 1^\circ$. Such a small value of ϑ_c , on the other hand, would imply a very short
 384 steep decay, in contradiction with observations.

385 **HLE from finite-duration pulse.** If we relax the assumption of infinitesimal duration of the
 386 pulse, we can assume that the jet continuously emits until it switches off at a radius R_0 . For the
 387 computation of the flux as a function of time we therefore integrate the comoving intensity along
 388 the equal-arrival-time surfaces (EATS)^{7,13,52,53}. Photons emitted at different times along the EATS
 389 arrive simultaneously to the observer. Using eq. (2) and imposing that $t_{obs}(\vartheta, R) = \text{const}$, the
 390 polar equation which describes the EATS is given by:

$$R(\vartheta, t_{obs}) = \frac{\beta c t_{obs}}{1 - \beta \cos \vartheta} \quad (12)$$

391 where we have expressed the emission time as $t_{em} = R/\beta c$, in the assumption of constant expan-
 392 sion velocity. From the above equation, we see that our assumption that the emission switches off

393 when the radius crosses R_0 translates to a ϑ -dependent switching off in the observer frame. At any
 394 time $t_{obs} > (1 - \beta)R_0/\beta c$, the observer receives the photons emitted along a surface given by the
 395 intersection of the EATS and the jet cone, defined by $R < R_0$, $\vartheta < \vartheta_j$ and $0 < \phi < 2\pi$, where ϕ is
 396 the azimuth angle. The resulting surface extends from a minimum angle $\vartheta_{min}(t_{obs})$ out to $\vartheta = \vartheta_j$,
 397 where the former is given by

$$\vartheta_{min}(t_{obs}) = \arccos\left(\frac{1}{\beta} - \frac{ct_{obs}}{R_0}\right) \quad (13)$$

398 The flux density is given by

$$F_\nu(t_{obs}) = \int_{\text{EATS}} I_\nu(\vartheta_{obs}) \cos(\vartheta_{obs}) d\Omega_{obs} \quad (14)$$

399 where I_ν is the specific intensity and $d\Omega_{obs}$ is the solid angle in the observer frame. Transforming
 400 to the comoving frame we have $I_\nu(\nu) = \mathcal{D}^3 I'_{\nu'}(\nu'/\mathcal{D})$. We decompose the comoving intensity as

$$I'_{\nu'} = I'_{\nu'_p} \cdot S_{\nu'} \quad (15)$$

401 where $I'_{\nu'_p}$ is the comoving intensity at the peak frequency ν'_p and $S_{\nu'}$ is the comoving spectral
 402 shape, normalized so that $S_{\nu'}(\nu'_p) = 1$. In general, $I'_{\nu'_p} \propto N_{tot}/R^2$, where N_{tot} is the number
 403 of emitting particles. If the emission process is synchrotron, $I'_{\nu'_p}$ is also proportional to B , the
 404 magnetic field as measured by an observer comoving with the jet, which is assumed to evolve as
 405 $B = B_0(R/R_0)^{-\lambda}$, with $\lambda \geq 0$ is a free parameter. If we assume N_{tot} to be constant in time, then
 406 $I'_{\nu'_p} \propto R^{-2}$ and, since $d\Omega_{obs} \propto R^2 \sin \vartheta$, the final form of the integral is

$$F_\nu(t_{obs}) \propto \int_{\vartheta_{min}(t_{obs})}^{\vartheta_j} S_{\nu'}(\nu'/\mathcal{D}(\vartheta)) \left(\frac{R(\vartheta, t_{obs})}{R_0}\right)^{-\lambda} \mathcal{D}^3(\vartheta) \sin \vartheta \cos \vartheta d\vartheta \quad (16)$$

407 The $\alpha - F$ relation for several values of λ is plotted in Fig. S4.

408 **HLE from an accelerating shell.** In this section we test the effect of relaxing the assumption that
 409 the shell which generates HLE expands with a constant bulk Lorentz factor Γ ^{14,54,55,56}. For our
 410 treatment we consider that the emission starts at $R = R_{in}$ and finishes at $R = R_{off}$. We assume
 411 also that Γ evolves as a power law with the radius, namely

$$\Gamma(R) = \Gamma_0 \left(\frac{R}{R_{in}}\right)^k \quad (17)$$

412 with $k > 0$ if the shell accelerates or $k < 0$ if the shell decelerates. We consider the emission
 413 of a photon at radius R_{em} and an angle $\vartheta = \vartheta_{em}$, then we define Δt_{em} the time necessary to
 414 expand from R_{in} to R_{em} . During the same interval of time, a photon emitted at radius R_{in} and
 415 an angle $\vartheta = 0$ travels a distance $c\Delta t_{em}$. Therefore the delay between these two photons is
 416 $\Delta t_{obs} = (R_{in} + c\Delta t_{em} - R_{em} \cos \vartheta)/c$. From eq. (17) we can write

$$\frac{1}{\sqrt{1 - \frac{1}{c^2} \frac{dR}{dt}}} = \Gamma_0 \left(\frac{R}{R_{in}}\right)^k \quad (18)$$

417 from which we derive

$$\frac{dR}{\sqrt{1 - \frac{1}{\Gamma_0^2} \left(\frac{R}{R_{in}}\right)^{-2k}}} = c dt \quad (19)$$

418 In the limit of $\Gamma_0 \gg \left(\frac{R}{R_{in}}\right)^{-k}$, we can write

$$\int_{R_{in}}^{R_{em}} \left[1 + \frac{1}{2\Gamma_0^2} \left(\frac{R}{R_{in}}\right)^{-2k} \right] dR \simeq c\Delta t_{em} \quad (20)$$

419 Thus, the delay time is

$$\Delta t_{obs} = \frac{R_{em}}{c}(1 - \cos \theta) + \frac{1}{2c} \int_{R_{in}}^{R_{em}} \frac{1}{\Gamma^2} dR \quad (21)$$

420 Given an arrival time Δt_{obs} , this equation allow us to associate a radius R_{em} to each angle ϑ_{em}
421 through the following expression:

$$\cos \vartheta_{em} = 1 - \frac{c\Delta t_{obs}}{R_{em}} + \frac{R_{in}}{2R_{em}} \frac{1}{\Gamma_0^2} \frac{1}{1 - 2k} \left[\left(\frac{R_{em}}{R_{in}}\right)^{1-2k} - 1 \right] \quad (22)$$

422 Inverting this equation, we obtain the polar equation $R_{em}(\vartheta_{em}, \Delta t_{obs})$ which defines the EATS,
423 namely all the photons emitted on this locus of points arrive to the observer with a time delay
424 Δt_{obs} with respect to the first photon coming from $R = R_{in}$ and $\vartheta = 0$. The computation of flux as
425 a function of time is again done using eq. (16), with the only difference that now β and Γ , which
426 appear in the Doppler factor $\mathcal{D}(\vartheta)$, depend on $R(\vartheta)$. The light curve and the spectral evolution for
427 values of k in the range $-0.4 \leq k \leq 0.4$ are showed in Fig. S5.

428 **Alternative scenarios shaping the X-ray tails.** In this section we explore other possible models of
429 prompt emission which can drive the evolution during the X-ray tails. We consider an anisotropic
430 jet core, for instance, made of mini jets⁵⁸ with angular sizes of $< 1/\Gamma$, with different comoving
431 spectra and bulk motion⁵⁹. In this case, the overall velocity and spectral distribution of mini-jets
432 should be the same for all the GRBs and a fine tuning is necessary to reproduce the $\alpha - F$ relation.
433 Moreover the small aperture angle of the mini-jets would produce very early a shallow segment due
434 to jet structure⁴⁰, in contradiction with the typical duration of X-ray tails. Within the HLE scenario,
435 only models which assume a dissipation occurring above the jet photosphere, such as in internal
436 shocks¹² or in magnetic reconnection scenarios^{57,60}, are able to reproduce the typical duration of
437 X-ray tails (~ 100 s). Photospheric models⁶¹, where dissipation occurs at radii $R_{ph} \sim 10^{12}$ cm⁶²,
438 give smaller times scales of $\sim 10^{-2}$ s, incompatible with observations. Only a common declining
439 activity of the central engine^{63,64} and a fine-tuned intrinsic spectral softening⁶⁵ would be required
440 to account for the $\alpha - F$ relation.

441 **Adiabatic Cooling.** In this section we derive the effect of adiabatic cooling of the emitting parti-
442 cles⁶⁶ on the light curve and the spectral evolution of X-ray tails. We assume that the emission is

443 dominated by a single species of particles that can be treated as a relativistic gas in adiabatic ex-
 444 pansion. We assume also that there is no interaction with other species of particles. If the particles
 445 are embedded in a region of comoving volume V' , an adiabatic expansion satisfies the equation

$$\langle \gamma \rangle^3 V' = \text{const} \quad (23)$$

446 where $\langle \gamma \rangle$ is the average Lorentz factor of the emitting particles in the comoving frame. The last
 447 equation is valid in the limit in which the adiabatic cooling timescale is smaller than the cooling
 448 time of other radiative processes, such as synchrotron or inverse Compton. Namely, particles radiate
 449 only a negligible fraction of their internal energy during the expansion of the system. Regarding
 450 the radial dependence of the volume V' , we distinguish two cases:

451 1) thick shell, with a comoving width $\Delta R'$ that does not evolve in time, hence $V' \propto R^2 \Delta R' \propto R^2$
 452 2) thin shell, with a comoving width $\Delta R'$ that evolves linearly with R , hence $V' \propto R^2 \Delta R' \propto R^3$.
 453 We assume that the dominant radiative process is synchrotron. The evolution of the spectrum in the
 454 observer frame is therefore fully determined once we know how the spectrum normalization F_{ν_p}
 455 and the peak frequency ν_p evolve in time. These two quantities, under the assumption of constant
 456 total number of emitting particles and constant bulk Lorentz factor Γ , take the following form:

$$F_{\nu_p} \propto B, \quad \nu_p \propto \langle \gamma \rangle^2 B \quad (24)$$

457 where B is the magnetic field (assumed tangled) as measured by a comoving observer. As de-
 458 scribed in the main text, we adopt the following parametrization for the magnetic field:

$$B = B_0 \left(\frac{R}{R_0} \right)^{-\lambda} \quad (25)$$

459 where $\lambda \geq 0$, under the reasonable assumption that magnetic field has to decrease or at most
 460 remain constant during the expansion. The value of R_0 corresponds to the radius where particles
 461 are injected, namely when adiabatic cooling starts to dominate. As before, we use the integration
 462 along the EATS defined in eq. (12) to compute the evolution of flux, with the only difference that
 463 in this case the emission never switches off. The final form of the integral is

$$F_{\nu}(t_{obs}) \propto \int_0^{\vartheta_j} S_{\nu'}(\nu/\mathcal{D}(\vartheta)) \left(\frac{R(\vartheta, t_{obs})}{R_0} \right)^{-\lambda} \mathcal{D}^3(\vartheta) \sin \vartheta \cos \vartheta d\vartheta \quad (26)$$

464 where the factor $(R/R_0)^{-\lambda}$ comes from $I'_{\nu'_p} \propto B$, while ν'_p evolves in time according to eq. (24).
 465 As stated before, HLE and adiabatic cooling have the same timescale, but the relevance of one
 466 process with respect to the other is determined by the decay of the magnetic field, which governs
 467 the drop of the spectrum normalization. The expected value of λ can be derived in several sce-
 468 narios, according to the process that rules the magnetic field evolution. In case of conservation of
 469 magnetic flux, the perpendicular and parallel component of B evolve as $B_{\perp} \sim 1/(\Delta R' \cdot r)$ and
 470 $B_{\parallel} \sim r^{-2}$, where r is the transverse radial dimension of the jet in a cylindrical reference system
 471 (r, ϕ, z) . If the jet is conical then $r \propto R$, leading to $B \sim R^{-1}$ ($\lambda = 1$) for $\Delta R' = \text{const}$ and
 472 $B \sim R^{-2}$ ($\lambda = 2$) for $\Delta R' \propto R$. Another possibility predicts equipartition between magnetic

473 energy density and particle energy density, giving $B^2 \sim \langle \gamma \rangle / V \sim V^{-4/3}$, where in the last step
474 we used eq. (23). In this case $B \sim R^{-4/3}$ ($\lambda = 4/3$) for $\Delta R' = \text{const}$ and $B \sim R^{-2}$ ($\lambda = 2$) for
475 $\Delta R' \propto R$. All these predicted values of λ are larger than the range found from our analysis. Such
476 tension can be solved, for instance, if the shell thickness decreases as the jet expands, or if the jet
477 is not conical (e.g. paraboloidal, with $r \propto \sqrt{R}$).

478 **References**

- 479
- 481 29. Paczynski, B., Rhoads, J. E. 1993. Radio Transients from Gamma-Ray Bursters. *The Astro-*
480 *physical Journal* 418, L5.
- 483 30. Mészáros, P., Rees, M. J. 1997. Optical and Long-Wavelength Afterglow from Gamma-Ray
484 Bursts. *The Astrophysical Journal* 476, 232.
- 485 31. Sari, R., Piran, T., Narayan, R. 1998. Spectra and Light Curves of Gamma-Ray Burst After-
486 glows. *The Astrophysical Journal* 497, L17.
- 487 32. Evans, P. A., and 24 colleagues 2009. Methods and results of an automatic analysis of a com-
488 plete sample of Swift-XRT observations of GRBs. *Monthly Notices of the Royal Astronomical*
489 *Society* 397, 1177.
- 490 33. Lien, A., and 14 colleagues 2016. The Third Swift Burst Alert Telescope Gamma-Ray Burst
491 Catalog. *The Astrophysical Journal* 829, 7.
- 492 34. Arnaud, K.A., 1996, *Astronomical Data Analysis Software and Systems V*, eds. G. Jacoby
493 and J. Barnes, p17, ASP Conf. Series volume 101.
- 494 35. Wilms, J., Allen, A., & McCray, R. 2000. On the Absorption of X-Rays in the Interstellar
495 Medium. *The Astrophysical Journal*, 542, 914
- 496 36. Kalberla, P. M. W., and 6 colleagues 2005. The Leiden/Argentine/Bonn (LAB) Survey of
497 Galactic HI. Final data release of the combined LDS and IAR surveys with improved stray-
498 radiation corrections. *Astronomy and Astrophysics* 440, 775.
- 499 37. Butler, N. R., Kocevski, D. 2007. X-Ray Hardness Evolution in GRB Afterglows and Flares:
500 Late-Time GRB Activity without N_H Variations. *The Astrophysical Journal* 663, 407.
- 501 38. Mu, H.-J., Lin, D.-B., Xi, S.-Q., et al. 2016. The History of GRB Outflows: Ejection Lorentz
502 Factor and Radiation Location of X-Ray Flares. *The Astrophysical Journal*, 831, 111
- 503 39. Perna, R., Lazzati, D. 2002. Time-dependent Photoionization in a Dusty Medium. I. Code
504 Description and General Results. *The Astrophysical Journal* 580, 261.
- 505 40. Oganessian, G., Ascenzi, S., Branchesi, M., Salafia, O. S., Dall’Osso, S., Ghirlanda, G. 2020.
506 Structured Jets and X-Ray Plateaus in Gamma-Ray Burst Phenomena. *The Astrophysical Jour-*
507 *nal* 893, 88.

- 508 41. Lin, D.-B., and 7 colleagues 2017. Steep Decay Phase Shaped by the Curvature Effect. II.
509 Spectral Evolution. *The Astrophysical Journal* 840, 118.
- 510 42. Rybicki, G. B., & Lightman, A. P. 1979. *Radiative Processes in Astrophysics*. A Wiley-
511 Interscience Publication
- 512 43. Kumar, P., & McMahon, E. 2008. A general scheme for modelling γ -ray burst prompt emission
513 . *Monthly Notices of the Royal Astronomical Society*, 384, 33
- 514 44. Beniamini, P., & Piran, T. 2013. Constraints on the Synchrotron Emission Mechanism in
515 Gamma-Ray Bursts . *The Astrophysical Journal*, 769, 69
- 516 45. Beniamini, P., Barniol Duran, R., & Giannios, D. 2018. Marginally fast cooling synchrotron
517 models for prompt GRBs . *Monthly Notices of the Royal Astronomical Society*, 476, 1785
- 518 46. Oganessian, G., Nava, L., Ghirlanda, G., et al. 2017. Detection of Low-energy Breaks in
519 Gamma-Ray Burst Prompt Emission Spectra. *The Astrophysical Journal*, 846, 137
- 520 47. Oganessian, G., Nava, L., Ghirlanda, G., et al. 2018. Characterization of gamma-ray burst
521 prompt emission spectra down to soft X-rays. *Astronomy and Astrophysics*, 616, A138
- 522 48. Oganessian, G., Nava, L., Ghirlanda, G., et al. 2019. Prompt optical emission as a signature of
523 synchrotron radiation in gamma-ray bursts. *Astronomy and Astrophysics*, 628, A59
- 524 49. Ravasio, M. E., Oganessian, G., Ghirlanda, G., et al. 2018. Consistency with synchrotron
525 emission in the bright GRB 160625B observed by Fermi. *Astronomy and Astrophysics*, 613,
526 A16
- 527 50. Ravasio, M. E., Ghirlanda, G., Nava, L., et al. 2019. Evidence of two spectral breaks in the
528 prompt emission of gamma-ray bursts. *Astronomy and Astrophysics*, 625, A60
- 529 51. Burgess, J. M., Bégué, D., Greiner, J., et al. 2020. Gamma-ray bursts as cool synchrotron
530 sources. *Nature Astronomy*, 4, 174
- 531 52. Dermer, C. D. 2004. Curvature Effects in Gamma-Ray Burst Colliding Shells. *The Astrophys-
532 ical Journal* 614, 284.
- 533 53. Salafia, O. S., Ghisellini, G., Pescalli, A., Ghirlanda, G., Nappo, F. 2016. Light curves and
534 spectra from off-axis gamma-ray bursts. *Monthly Notices of the Royal Astronomical Society*
535 461, 3607.
- 536 54. Uhm, Z. L., Zhang, B. 2016. Evidence of Bulk Acceleration of the GRB X-Ray Flare Emission
537 Region. *The Astrophysical Journal* 824, L16.
- 538 55. Uhm, Z. L., Zhang, B. 2016. Toward an Understanding of GRB Prompt Emission Mechanism.
539 I. The Origin of Spectral Lags. *The Astrophysical Journal* 825, 97.

- 540 56. Uhm, Z. L., Zhang, B., Racusin, J. 2018. Toward an Understanding of GRB Prompt Emission
541 Mechanism. II. Patterns of Peak Energy Evolution and Their Connection to Spectral Lags. *The*
542 *Astrophysical Journal* 869, 100.
- 543 57. Lyutikov, M., Blandford, R. 2003. Gamma Ray Bursts as Electromagnetic Outflows. arXiv
544 e-prints astro-ph/0312347.
- 545 58. Narayan, R., & Kumar, P. 2009. A turbulent model of gamma-ray burst variability. *Monthly*
546 *Notices of the Royal Astronomical Society*, 394, L117
- 547 59. Barniol Duran, R., Leng, M., Giannios, D. 2016. An anisotropic minijets model for the GRB
548 prompt emission. *Monthly Notices of the Royal Astronomical Society* 455, L6.
- 549 60. Drenkhahn, G., Spruit, H. C. 2002. Efficient acceleration and radiation in Poynting flux powered
550 GRB outflows. *Astronomy and Astrophysics* 391, 1141.
- 551 61. Pe'er, A. 2008. Temporal Evolution of Thermal Emission from Relativistically Expanding
552 Plasma. *The Astrophysical Journal* 682, 463.
- 553 62. Piran, T. 1999. Gamma-ray bursts and the fireball model. *Physics Reports* 314, 575.
- 554 63. Kumar, P., Narayan, R., & Johnson, J. L. 2008, Properties of Gamma-Ray Burst Progenitor
555 Stars, *Science*, 321, 376
- 556 64. Hascoët, R., Daigne, F., Mochkovitch, R. 2012. Accounting for the XRT early steep decay in
557 models of the prompt gamma-ray burst emission. *Astronomy and Astrophysics* 542, L29.
- 558 65. Beloborodov, A. M. 2011. Radiative Transfer in Ultrarelativistic Outflows. *The Astrophysical*
559 *Journal* 737, 68.
- 560 66. Panaitescu, A. 2019. Adiabatic and Radiative Cooling of Relativistic Electrons Applied to
561 Synchrotron Spectra and Light Curves of Gamma-Ray Burst Pulses. *The Astrophysical Jour-*
562 *nal*, 886, 106

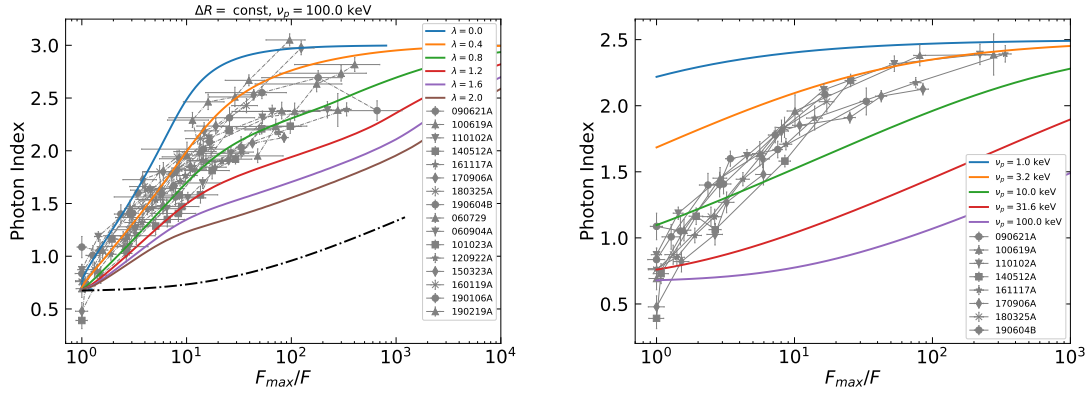


Figure S1: **Left panel:** Spectral evolution expected in case of adiabatic cooling (solid lines) superimposed to the first and the second sample. The theoretical curves are computed taking also into account the effect of HLE. The value of λ specifies the evolution of the magnetic field. We adopt a SBPL as spectral shape with $\alpha_s = -1/3$ and $\beta_s = 2.0$, an initial observed peak frequency of 100 keV and a thickness of the expanding shell that is constant in time. The dot-dashed line is the evolution expected considering only HLE, assuming the same spectral shape and initial observed peak frequency. **Right panel:** Spectral evolution expected for HLE from an infinitesimal duration pulse, with the assumption of a SBPL spectrum. The several colors indicate the observed peak frequency at the beginning of the decay.

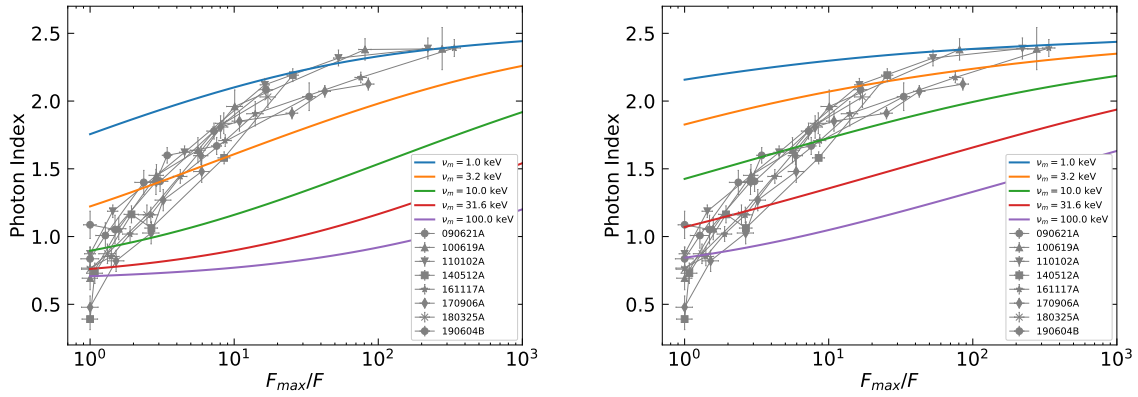


Figure S2: **Left panel:** Spectral evolution expected for HLE from a infinitesimal duration pulse, with the assumption of a synchrotron spectrum with $\nu_m/\nu_c = 1$. The several colors indicate the observed peak frequency at the beginning of the decay. **Right panel:** Spectral evolution expected for HLE from a infinitesimal duration pulse, with the assumption of a synchrotron spectrum with $\nu_m/\nu_c = 10$. The several colors indicate the observed peak frequency at the beginning of the decay. The spectral evolution appears slightly steeper with respect to the case $\nu_m/\nu_c = 1$ because for $\nu_c < \nu < \nu_m$ the spectrum goes like $F_\nu \sim \nu^{-p/2}$.

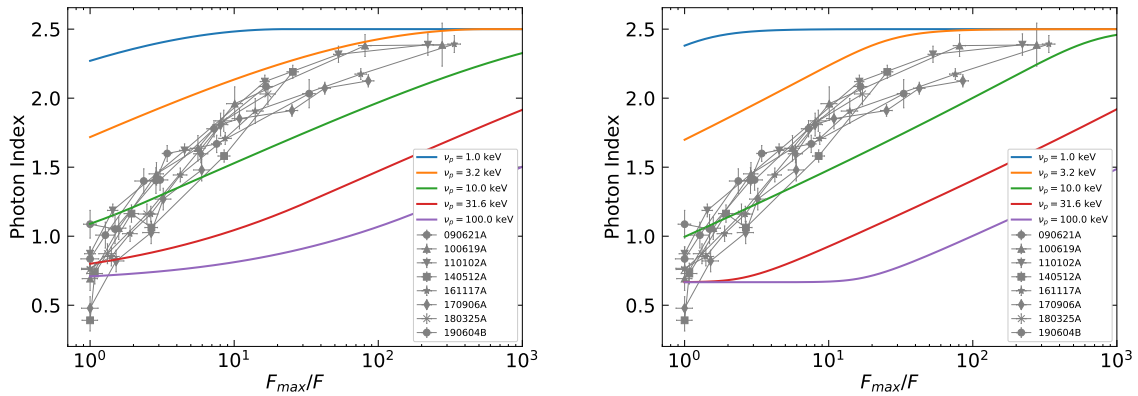


Figure S3: **Left panel:** HLE for a Band function as spectral shape. **Right panel:** Spectral evolution expected for HLE from a infinitesimal duration pulse, with the assumption of a SBPL with sharpness parameter $n = 4$ as spectral shape.

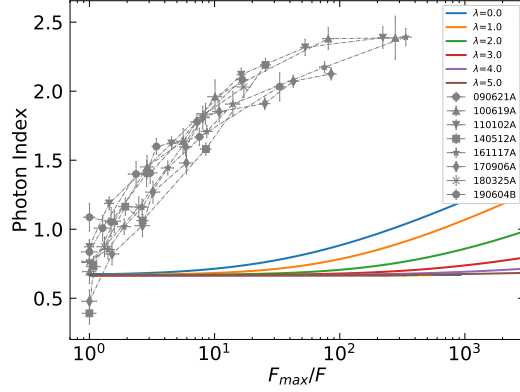


Figure S4: Spectral evolution in case of HLE from a finite-duration pulse. The adopted parameters are $R_{in} = 3 \times 10^{15}$ cm, $R_{off} = 9 \times 10^{15}$ cm, $\Gamma_0 = 100$ and $\nu_p = 100$ keV. The adopted spectral shape is a SBPL.

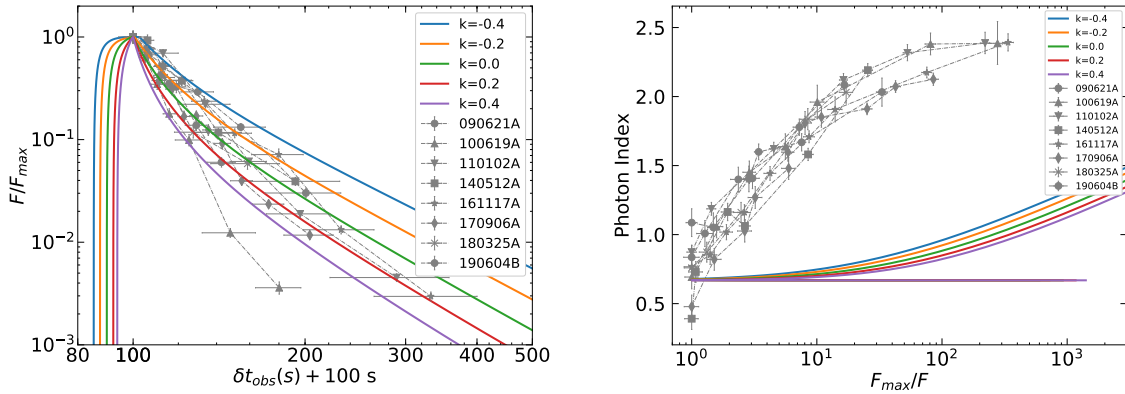


Figure S5: **Left panel:** Light curve of HLE from a finite-duration pulse, in case of not constant Γ . The magnetic field does not evolve with radius, i.e $\lambda = 0$. The adopted parameters are $R_{in} = 3 \times 10^{15}$ cm, $R_{off} = 9 \times 10^{15}$ cm, $\Gamma_0 = 100$ and $\nu_p = 100$ keV. The adopted spectral shape is a SBPL. The peak of each curve is shifted at 100 s. **Right panel:** Spectral evolution in case of HLE from a finite-duration pulse, in case of not constant Γ . The magnetic field does not evolve with radius, i.e $\lambda = 0$. The adopted parameters are $R_{in} = 3 \times 10^{15}$ cm, $R_{off} = 9 \times 10^{15}$ cm, $\Gamma_0 = 100$ and $\nu_p = 100$ keV. The adopted spectral shape is a SBPL.

name	z	$N_H(10^{22}cm^{-2})$	$T_i(s)$	$T_f(s)$
090621A	-	1.53	268	369
100619A	-	0.46	88	168
110102A	-	0.14	266	455
140512A	0.725	0.12	124	216
161117A	1.549	0.58	121	353
170906A	-	0.23	90	194
180325A	2.25	0.71	87	146
190604B	-	0.21	219	262

Table S1: Main information about the GRBs of the first sample. z is the redshift, when available. N_H is the column density adopted in the spectral analysis of the X-ray tail. T_i and T_f are the central times of the initial and final bins of the spectral analysis, respectively.

name	z	$N_H(10^{22}cm^{-2})$	$T_i(s)$	$T_f(s)$	$T_p^{BAT}(s)$
060729	0.54	0.03	133	163	93
060904A	-	0.13	74	148	56
101023A	-	0.17	91	180	63
120922A	-	0.09	128	296	100
150323A	0.593	0.44	153	241	136
160119A	-	0.14	166	267	147
190106A	1.86	0.68	99	227	76
190219A	-	0.14	114	186	66

Table S2: Main information about the GRBs of the second sample. z is the redshift, when available. N_H is the column density adopted in the spectral analysis of the X-ray tail. T_i and T_f are the central times of the initial and final bins of the spectral analysis, respectively. $T_p^{BAT}(s)$ is the peak time of the BAT pulse preceding the X-ray tail, used for the extrapolation of F_{max}

GRB	time sec	α -	$F_{(0.5-10)}$ keV 10^{-10} erg cm $^{-2}$ s $^{-1}$	cstat/dof -
090621A				
	265 – 271	$1.09^{+0.1}_{-0.1}$	$397.6^{+19.7}_{-20.5}$	321.3/377
	271 – 278	$1.05^{+0.11}_{-0.11}$	$267.0^{+13.9}_{-14.6}$	282.7/351
	278 – 289	$1.4^{+0.09}_{-0.09}$	$138.8^{+6.0}_{-6.2}$	274.8/381
	289 – 306	$1.6^{+0.06}_{-0.06}$	$116.0^{+3.0}_{-3.1}$	509.3/548
	306 – 339	$1.67^{+0.06}_{-0.06}$	$52.6^{+1.5}_{-1.5}$	452.0/527
	339 – 399	$2.03^{+0.1}_{-0.1}$	$12.0^{+0.6}_{-0.6}$	253.7/346
100619A				
	85 – 90	$0.69^{+0.09}_{-0.08}$	$1311.0^{+77.8}_{-82.1}$	289.5/363
	90 – 95	$1.06^{+0.08}_{-0.08}$	$829.3^{+46.6}_{-49.1}$	259.4/347
	95 – 101	$1.45^{+0.08}_{-0.08}$	$454.1^{+23.8}_{-25.1}$	253.1/325
	101 – 106	$1.64^{+0.09}_{-0.09}$	$234.0^{+13.1}_{-13.7}$	233.5/277
	106 – 120	$1.96^{+0.12}_{-0.12}$	$130.0^{+8.4}_{-8.9}$	151.4/170
	120 – 152	$2.38^{+0.08}_{-0.08}$	$16.2^{+0.6}_{-0.6}$	267.6/320
	152 – 185	$2.39^{+0.15}_{-0.16}$	$4.7^{+0.4}_{-0.4}$	130.9/164
110102A				
	260 – 272	$0.87^{+0.05}_{-0.05}$	$484.3^{+20.5}_{-21.3}$	462.9/524
	272 – 286	$1.19^{+0.05}_{-0.05}$	$337.0^{+13.1}_{-13.6}$	463.2/485
	286 – 314	$1.62^{+0.05}_{-0.05}$	$107.0^{+3.8}_{-4.0}$	451.9/424
	314 – 337	$2.12^{+0.05}_{-0.05}$	$29.7^{+0.9}_{-0.9}$	324.3/386
	337 – 387	$2.32^{+0.06}_{-0.06}$	$9.1^{+0.3}_{-0.3}$	265.6/354
	387 – 523	$2.39^{+0.08}_{-0.08}$	$2.2^{+0.1}_{-0.1}$	272.9/299
140512A				
	121 – 127	$0.39^{+0.08}_{-0.08}$	$347.3^{+21.1}_{-22.1}$	279.3/414
	127 – 133	$0.73^{+0.08}_{-0.08}$	$322.2^{+20.1}_{-21.2}$	271.6/359
	133 – 140	$1.16^{+0.06}_{-0.06}$	$179.3^{+9.1}_{-9.5}$	388.3/416
	140 – 151	$1.06^{+0.05}_{-0.05}$	$130.4^{+5.0}_{-5.1}$	482.6/530
	151 – 179	$1.58^{+0.04}_{-0.04}$	$40.8^{+1.4}_{-1.4}$	459.8/480
	179 – 254	$2.19^{+0.05}_{-0.05}$	$13.6^{+0.4}_{-0.4}$	383.2/419

Table S3: Results of time resolved spectral analysis for the first sample of GRBs. For each bin we report the time window, the photon index α , the un-absorbed flux $F_{(0.5-10)}$ keV and the statistic over the degrees of freedom (dof).

GRB	time sec	α -	$F_{(0.5-10)} \text{ keV}$ $10^{-10} \text{ erg cm}^{-2} \text{ s}^{-1}$	cstat/dof -
161117A				
	118 – 123	$0.77^{+0.08}_{-0.08}$	$1132.5^{+73.9}_{-77.8}$	295.9/358
	123 – 130	$0.85^{+0.07}_{-0.07}$	$806.3^{+49.0}_{-51.4}$	320.9/371
	130 – 138	$1.02^{+0.06}_{-0.06}$	$597.6^{+29.1}_{-30.5}$	320.6/440
	138 – 147	$1.16^{+0.06}_{-0.06}$	$429.2^{+20.9}_{-21.6}$	343.5/427
	147 – 161	$1.44^{+0.05}_{-0.05}$	$267.9^{+11.1}_{-11.5}$	378.2/422
	161 – 182	$1.71^{+0.04}_{-0.04}$	$130.7^{+4.2}_{-4.4}$	399.9/458
	182 – 219	$1.91^{+0.09}_{-0.09}$	$80.9^{+5.0}_{-5.4}$	190.8/202
	219 – 285	$2.17^{+0.04}_{-0.04}$	$15.0^{+0.4}_{-0.4}$	390.1/465
	285 – 421	$2.39^{+0.06}_{-0.06}$	$3.4^{+0.1}_{-0.1}$	290.3/335
170906A				
	88 – 93	$0.48^{+0.08}_{-0.08}$	$1936.6^{+124.7}_{-132.6}$	264.0/331
	93 – 98	$0.82^{+0.08}_{-0.08}$	$1277.8^{+78.1}_{-83.0}$	272.8/330
	98 – 105	$1.03^{+0.08}_{-0.08}$	$729.9^{+45.3}_{-48.2}$	235.2/309
	105 – 110	$1.27^{+0.08}_{-0.08}$	$601.6^{+35.4}_{-37.7}$	246.0/299
	110 – 116	$1.48^{+0.08}_{-0.08}$	$325.3^{+18.4}_{-19.5}$	223.0/284
	116 – 123	$1.6^{+0.06}_{-0.07}$	$329.1^{+15.0}_{-15.7}$	304.6/337
	123 – 129	$1.81^{+0.08}_{-0.08}$	$240.6^{+12.6}_{-13.2}$	239.4/256
	129 – 139	$1.85^{+0.07}_{-0.07}$	$178.0^{+8.4}_{-8.8}$	239.7/292
	139 – 152	$1.91^{+0.04}_{-0.04}$	$76.9^{+2.1}_{-2.1}$	414.8/440
	152 – 174	$2.07^{+0.04}_{-0.04}$	$45.5^{+1.2}_{-1.2}$	365.0/443
	174 – 215	$2.13^{+0.04}_{-0.04}$	$22.7^{+0.6}_{-0.6}$	393.1/421
180325A				
	85 – 90	$0.76^{+0.07}_{-0.07}$	$193.7^{+12.4}_{-13.2}$	262.1/384
	90 – 96	$0.87^{+0.07}_{-0.07}$	$146.7^{+9.5}_{-10.1}$	289.9/349
	96 – 106	$1.16^{+0.07}_{-0.07}$	$78.1^{+5.1}_{-5.3}$	237.4/325
	106 – 124	$1.84^{+0.08}_{-0.08}$	$22.9^{+1.3}_{-1.4}$	267.5/274
	124 – 168	$2.03^{+0.08}_{-0.08}$	$11.3^{+0.6}_{-0.7}$	229.5/268
190604B				
	216 – 222	$0.84^{+0.09}_{-0.09}$	$1460.4^{+100.1}_{-107.2}$	247.5/297
	222 – 228	$1.01^{+0.09}_{-0.09}$	$1144.3^{+84.0}_{-89.8}$	219.1/252
	228 – 234	$1.4^{+0.09}_{-0.09}$	$619.1^{+40.2}_{-43.1}$	251.5/255
	234 – 243	$1.41^{+0.07}_{-0.07}$	$477.2^{+26.5}_{-28.1}$	278.4/301
	243 – 254	$1.78^{+0.06}_{-0.06}$	$201.5^{+8.0}_{-8.4}$	327.9/346
	254 – 270	$2.08^{+0.06}_{-0.06}$	$87.8^{+3.0}_{-3.1}$	305.8/331

Table S4: -continued

GRB	time sec	α	$F_{(0.5-10) \text{ keV}}$ $10^{-10} \text{ erg cm}^{-2} \text{ s}^{-1}$	cstat/dof
<hr/>				
060729				
	130 – 135	$1.95^{+0.06}_{-0.07}$	$481.9^{+23.0}_{-24.4}$	266.9/265
	135 – 141	$2.23^{+0.08}_{-0.07}$	$323.7^{+15.8}_{-16.0}$	252.8/221
	141 – 147	$2.37^{+0.08}_{-0.08}$	$213.9^{+10.2}_{-10.6}$	220.7/202
	147 – 152	$2.63^{+0.07}_{-0.08}$	$131.9^{+5.5}_{-5.7}$	234.4/197
	152 – 159	$2.74^{+0.08}_{-0.08}$	$77.0^{+3.1}_{-3.2}$	232.0/203
	159 – 167	$2.82^{+0.07}_{-0.07}$	$57.1^{+1.9}_{-1.9}$	193.1/246
<hr/>				
060904A				
	72 – 77	$1.09^{+0.08}_{-0.08}$	$257.2^{+17.2}_{-18.2}$	245.7/294
	77 – 82	$1.19^{+0.08}_{-0.09}$	$220.5^{+15.8}_{-16.7}$	233.5/256
	82 – 88	$1.45^{+0.09}_{-0.09}$	$112.9^{+8.1}_{-8.7}$	172.7/239
	88 – 97	$1.55^{+0.05}_{-0.05}$	$71.0^{+3.0}_{-3.1}$	387.7/401
	97 – 109	$1.69^{+0.05}_{-0.05}$	$51.2^{+2.0}_{-2.1}$	369.1/378
	109 – 128	$1.98^{+0.06}_{-0.06}$	$27.6^{+1.1}_{-1.1}$	320.2/345
	128 – 168	$2.37^{+0.06}_{-0.06}$	$11.1^{+0.4}_{-0.4}$	249.3/298
<hr/>				
101023A				
	88 – 94	$1.29^{+0.08}_{-0.08}$	$294.0^{+18.7}_{-19.9}$	252.9/326
	94 – 99	$1.35^{+0.07}_{-0.07}$	$227.6^{+13.1}_{-13.8}$	289.7/331
	99 – 105	$1.41^{+0.08}_{-0.08}$	$178.4^{+11.0}_{-11.6}$	244.6/304
	105 – 110	$1.47^{+0.07}_{-0.07}$	$165.7^{+9.2}_{-9.7}$	298.3/319
	110 – 118	$1.58^{+0.08}_{-0.08}$	$109.9^{+6.4}_{-6.8}$	255.5/309
	118 – 127	$1.81^{+0.08}_{-0.08}$	$85.0^{+4.7}_{-5.0}$	280.8/291
	127 – 143	$1.92^{+0.05}_{-0.05}$	$50.8^{+1.6}_{-1.6}$	417.0/429
	143 – 168	$2.21^{+0.05}_{-0.05}$	$28.6^{+0.8}_{-0.8}$	341.2/399
	168 – 193	$2.23^{+0.07}_{-0.07}$	$15.3^{+0.6}_{-0.6}$	271.6/311

Table S5: Results of time resolved spectral analysis for the second sample of GRBs. For each bin we report the time window, the photon index α , the un-absorbed flux $F_{(0.5-10) \text{ keV}}$ and the statistic over the degrees of freedom (dof).

GRB	time sec	α -	$F_{(0.5-10)} \text{ keV}$ $10^{-10} \text{ erg cm}^{-2} \text{ s}^{-1}$	cstat/dof -
120922A				
	125 – 130	$1.09^{+0.07}_{-0.07}$	$374.2^{+22.8}_{-24.2}$	297.7/333
	130 – 136	$1.19^{+0.07}_{-0.07}$	$348.1^{+21.4}_{-22.6}$	304.4/321
	136 – 141	$1.32^{+0.08}_{-0.08}$	$251.9^{+16.9}_{-18.0}$	268.3/281
	141 – 146	$1.28^{+0.07}_{-0.07}$	$292.0^{+17.4}_{-18.3}$	280.1/316
	146 – 152	$1.46^{+0.08}_{-0.08}$	$203.0^{+13.3}_{-14.1}$	234.1/276
	152 – 157	$1.53^{+0.07}_{-0.07}$	$186.4^{+10.5}_{-11.0}$	263.6/294
	157 – 162	$1.58^{+0.07}_{-0.07}$	$168.2^{+9.4}_{-9.8}$	274.1/299
	162 – 170	$1.64^{+0.07}_{-0.07}$	$131.0^{+7.6}_{-8.0}$	239.0/286
	170 – 178	$1.77^{+0.06}_{-0.06}$	$97.7^{+4.8}_{-5.1}$	291.7/294
	178 – 188	$1.82^{+0.07}_{-0.07}$	$80.2^{+4.0}_{-4.2}$	250.9/297
	188 – 199	$1.91^{+0.06}_{-0.06}$	$65.7^{+3.0}_{-3.2}$	288.6/300
	199 – 212	$1.9^{+0.07}_{-0.07}$	$62.1^{+3.2}_{-3.3}$	233.5/282
	212 – 228	$1.84^{+0.04}_{-0.04}$	$50.9^{+1.5}_{-1.6}$	390.6/436
	228 – 247	$1.9^{+0.04}_{-0.04}$	$43.6^{+1.2}_{-1.3}$	341.0/444
	247 – 276	$1.99^{+0.04}_{-0.04}$	$28.0^{+0.8}_{-0.8}$	375.0/428
	276 – 316	$2.2^{+0.04}_{-0.04}$	$19.1^{+0.5}_{-0.5}$	320.7/399
150323A				
	150 – 156	$1.73^{+0.07}_{-0.07}$	$333.5^{+17.6}_{-18.6}$	238.1/282
	156 – 161	$1.8^{+0.09}_{-0.09}$	$211.7^{+12.4}_{-13.1}$	202.8/254
	161 – 167	$1.92^{+0.08}_{-0.08}$	$149.6^{+7.8}_{-8.3}$	251.2/276
	167 – 176	$2.19^{+0.08}_{-0.08}$	$86.4^{+3.9}_{-4.0}$	254.5/264
	176 – 190	$2.23^{+0.07}_{-0.07}$	$66.9^{+2.7}_{-2.8}$	242.1/300
	190 – 215	$2.53^{+0.05}_{-0.05}$	$29.0^{+0.7}_{-0.7}$	300.3/364
	215 – 267	$2.98^{+0.06}_{-0.07}$	$10.2^{+0.3}_{-0.3}$	251.2/298
160119A				
	164 – 169	$1.25^{+0.07}_{-0.07}$	$183.1^{+10.9}_{-11.4}$	279.0/347
	169 – 174	$1.37^{+0.08}_{-0.08}$	$171.7^{+10.7}_{-11.4}$	241.7/303
	174 – 180	$1.47^{+0.07}_{-0.07}$	$134.6^{+7.9}_{-8.4}$	219.9/320
	180 – 185	$1.54^{+0.07}_{-0.07}$	$109.8^{+6.3}_{-6.6}$	217.4/309
	185 – 193	$1.66^{+0.05}_{-0.05}$	$129.6^{+5.3}_{-5.5}$	323.5/389
	193 – 200	$1.63^{+0.06}_{-0.06}$	$126.9^{+5.6}_{-5.9}$	341.0/376
	200 – 209	$1.8^{+0.06}_{-0.06}$	$93.4^{+3.9}_{-4.1}$	347.9/370
	209 – 223	$1.94^{+0.06}_{-0.06}$	$63.6^{+2.5}_{-2.6}$	324.0/342
	223 – 242	$2.12^{+0.06}_{-0.06}$	$37.9^{+1.5}_{-1.5}$	292.8/326
	242 – 291	$2.43^{+0.07}_{-0.07}$	$13.8^{+0.5}_{-0.5}$	249.1/308

Table S6: -continued

GRB	time sec	α -	$F_{(0.5-10) \text{ keV}}$ $10^{-10} \text{ erg cm}^{-2} \text{ s}^{-1}$	cstat/dof -
190106A				
	96 – 101	$1.56^{+0.08}_{-0.08}$	$221.9^{+13.4}_{-14.4}$	247.0/263
	101 – 106	$2.02^{+0.09}_{-0.09}$	$120.6^{+7.5}_{-7.9}$	226.2/220
	106 – 114	$2.31^{+0.1}_{-0.1}$	$67.7^{+3.8}_{-4.0}$	150.5/198
	114 – 130	$2.55^{+0.06}_{-0.06}$	$33.2^{+1.0}_{-1.0}$	271.4/319
	130 – 181	$2.69^{+0.07}_{-0.07}$	$9.6^{+0.3}_{-0.3}$	359.4/332
	181 – 274	$2.38^{+0.09}_{-0.09}$	$2.6^{+0.1}_{-0.1}$	242.7/268
190219A				
	111 – 117	$1.99^{+0.08}_{-0.08}$	$99.8^{+5.3}_{-5.6}$	199.8/251
	117 – 124	$2.29^{+0.07}_{-0.07}$	$116.9^{+5.0}_{-5.1}$	218.2/267
	124 – 134	$2.46^{+0.07}_{-0.07}$	$82.8^{+3.4}_{-3.5}$	238.2/254
	134 – 146	$2.51^{+0.09}_{-0.09}$	$46.0^{+2.3}_{-2.3}$	188.4/215
	146 – 164	$2.67^{+0.05}_{-0.05}$	$33.8^{+0.9}_{-0.9}$	328.2/316
	164 – 208	$3.05^{+0.06}_{-0.06}$	$13.8^{+0.4}_{-0.4}$	295.2/306

Table S7: -continued

Figures

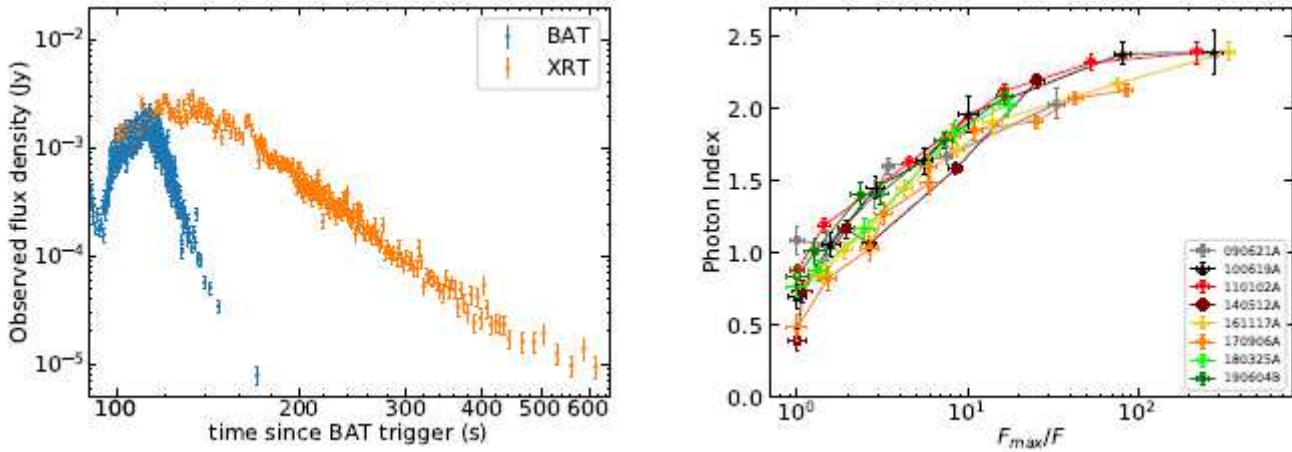


Figure 1

Left panel: An example of a light curve of an X-ray tail selected from our sample, taken from the GRB 161117A. We show on the same plot the XRT (orange) and the BAT (blue) flux density at 1 keV and 50 keV, respectively. Right panel: Spectral evolution of the X-ray tail for all the GRBs in the first sample (shown with different colors). The photon index α is represented as a function of the reciprocal of the normalized flux F_{max}/F . Time flows from left to right.

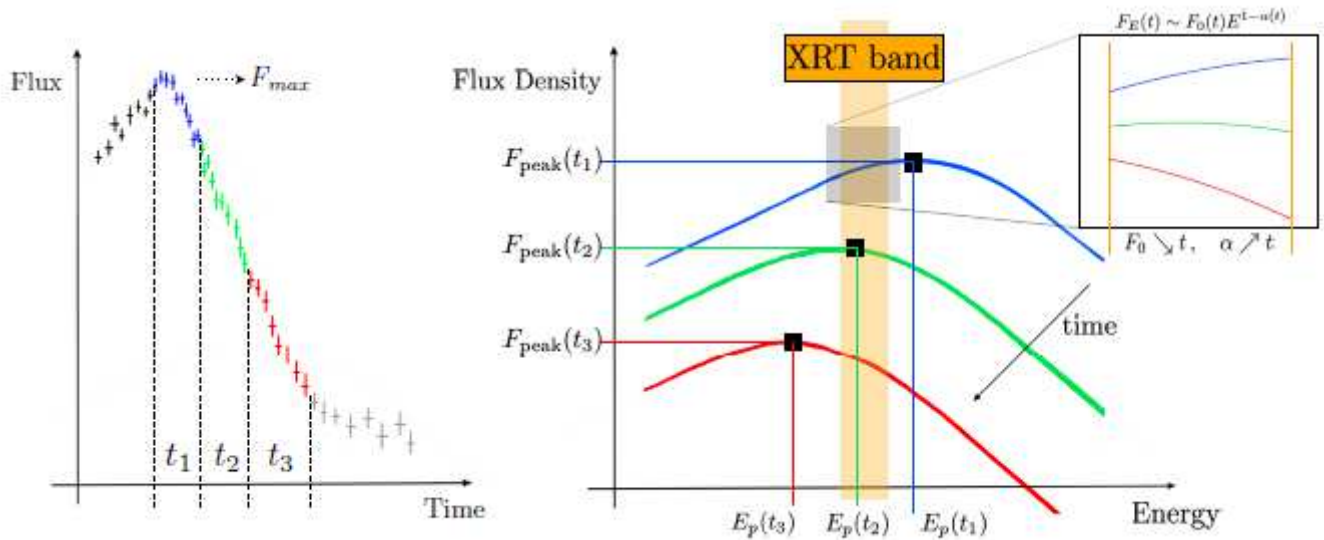


Figure 2

Illustration of the spectral evolution caused by a shift of the spectrum towards lower energies. The transition of the spectral peak through the XRT band explains the observed spectral softening. Since in the right panel we plot the flux density, the local slope in the XRT band is given by $1 - \alpha$, where α is the photon index.

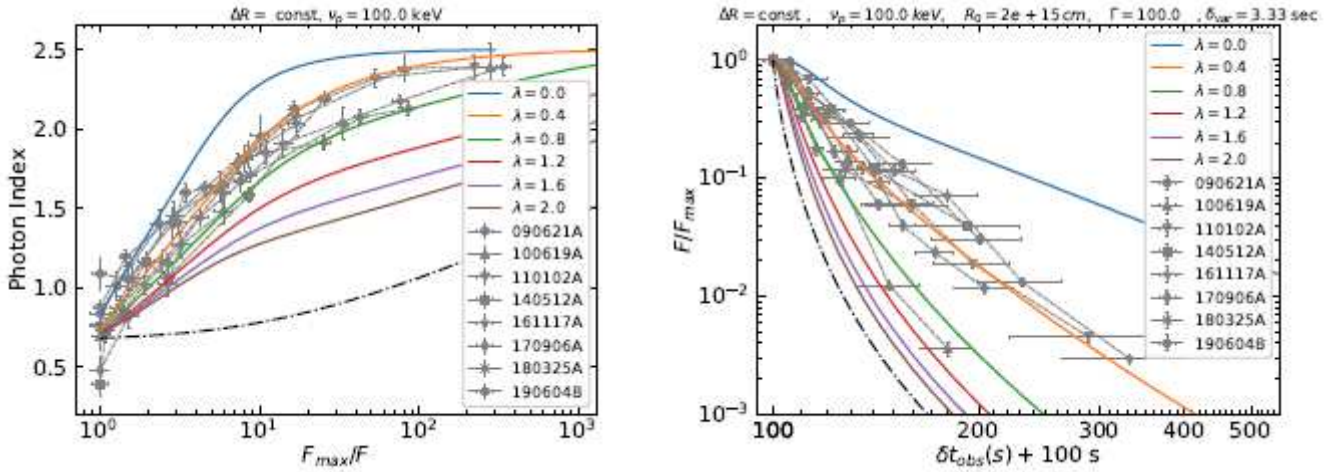


Figure 3

Left panel: Spectral evolution expected in the case of adiabatic cooling (solid lines). The theoretical curves are computed taking also into account the effect of HLE. The value of λ specifies the evolution of the magnetic field. We adopt a SBPL as spectral shape with $\alpha_s = -1/3$ and $\beta_s = 1.5$, an initial observed peak frequency of 100 keV and a thickness of the expanding shell that is constant in time. The dot-dashed line is the evolution expected in case of HLE without adiabatic cooling, assuming the same spectral shape and initial observed peak frequency. Right panel: Temporal evolution of normalized flux expected in case of adiabatic cooling. $\delta t_{obs} + 100 s$ is the time measured from the peak of the decay shifted at 100 s, the typical starting time of the tail emission detected by XRT. We adopt the same parameters as in the left panel, assuming $R_0 = 2 \times 10^{15} \text{ cm}$ and $\Gamma = 100$. The dot-dashed line is the corresponding HLE model without accounting for adiabatic cooling. $\delta t_{var} = R_0/2c\Gamma^2$ indicates the timescale of adiabatic cooling, which is the same of HLE.

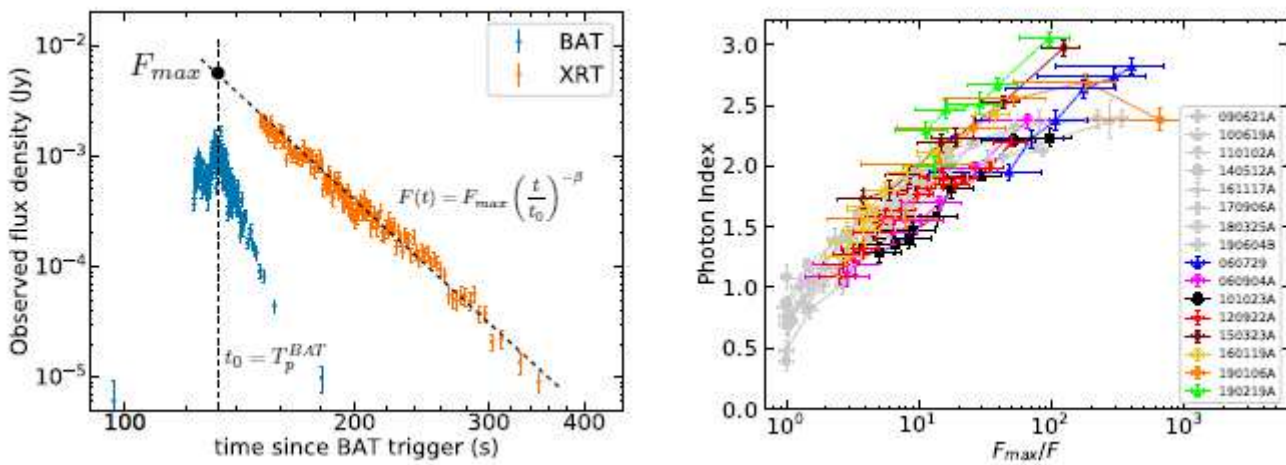


Figure 4

Left panel: An example of a light curve of an X-ray tail selected for our second sample, taken from GRB 150323A. We report on the same plot the XRT (orange) and the BAT (blue) flux density at 1 keV and 50

keV, respectively. The peak flux F_{\max} is estimated extrapolating the X-ray tail back to the BAT peak. Right panel: Spectral evolution of our extended sample of GRBs, which present a steep decay at the beginning of the XRT light curve, preceded by the brightest BAT pulse since the trigger time. The evolution of α lies on the same region of the plane occupied by the original sample, indicated in grey.